

1 **Climatological distribution of dissolved inorganic nutrients**

2 **in the Western Mediterranean Sea (1981-2017)**

3

4 **Malek Belgacem^{1,2}, Katrin Schroeder¹, Alexander Barth³, Charles Troupin³, Bruno**
5 **Pavoni², Patrick Rambault⁴, Nicole Garcia⁴, Mireno Borghini⁵, Jacopo Chiggiato¹**

6 ¹CNR-ISMAR, Arsenale Tesa 104, Castello 2737/F, 30122 Venezia, Italy

7 ²Dipartimento di Scienze Ambientali Informatica e Statistica, DAIS, Università Ca' Foscari
8 Venezia, Campus Scientifico Mestre, Italy

9 ³GeoHydrodynamics and Environment Research, GHER, Freshwater and Oceanic sCiences
10 Unit of reSearch (FOCUS), University of Liège, Quartier Agora, Allée du 6-Août, 17, Sart
11 Tilman, 4000 Liège 1, Belgium

12 ⁴Aix Marseille Université, CNRS/INSU, Université de Toulon, IRD, Mediterranean Institute of
13 Oceanography (MIO) UM 110, 13288, Marseille, France

14 ⁵CNR-ISMAR, La Spezia, Italy

15 Correspondence: Malek Belgacem (malek.belgacem@ve.ismar.cnr.it)

16 **Abstract**

17 The Western MEDiterranean Sea BioGeochemical Climatology (BGC-WMED) presented here is a
18 product derived from quality controlled in situ observations. Annual mean gridded nutrient fields for the
19 period 1981-2017, and its sub-periods 1981-2004 and 2005-2017, on a horizontal $1/4^\circ \times 1/4^\circ$ grid have
20 been produced. The biogeochemical climatology is built on 19 depth levels and for the dissolved
21 inorganic nutrients nitrate, phosphate and orthosilicate. To generate smooth and homogeneous
22 interpolated fields, the method of the Variational Inverse Model (VIM) was applied. A sensitivity
23 analysis was carried out to assess the comparability of the data product with the observational data. The
24 BGC-WMED has then been compared to other available data products, i.e. the medBFM
25 biogeochemical reanalysis of the Mediterranean Sea and the World Ocean Atlas 2018 (WOA18) (its
26 biogeochemical part). The new product reproduces common features with more detailed patterns and
27 agrees with previous records. This suggests a good reference to the region and to the scientific
28 community for the understanding of inorganic nutrient variability in the western Mediterranean Sea, in
29 space and in time, but our new climatology can also be used to validate numerical simulations making
30 it a reference data product.

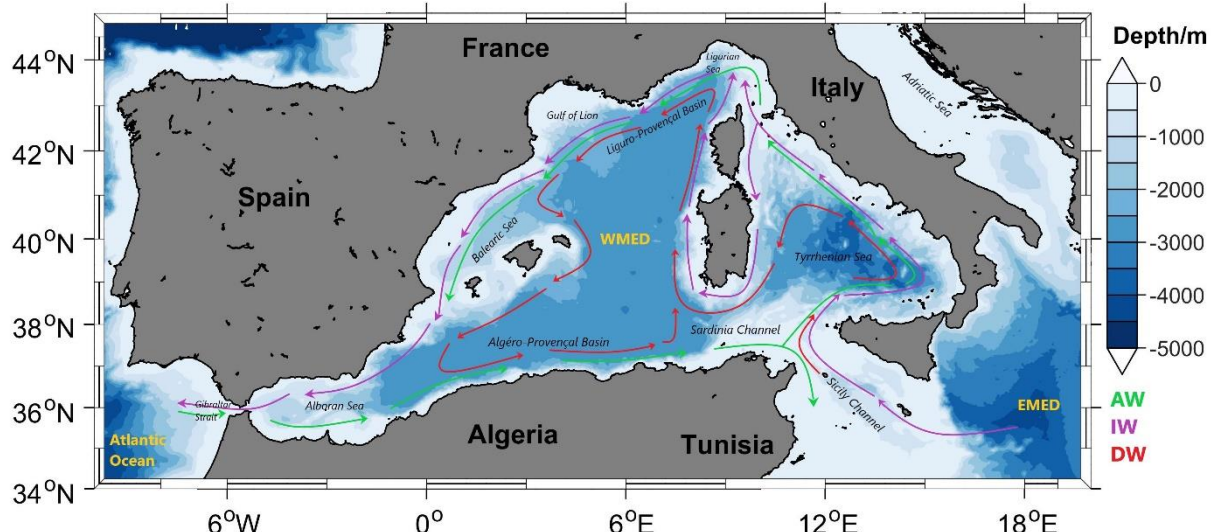
31 **Keywords:** Western Mediterranean Sea, climatology, inorganic nutrients, in situ observations.

32 **1 Introduction**

33 Ocean life relies on the loads of marine macro-nutrients (nitrate, phosphate and orthosilicate) and other
34 micro-nutrients within the euphotic layer. They fuel phytoplankton growth, maintaining thus the
35 equilibrium of the food web. These nutrients may reach deeper levels through vertical mixing and
36 remineralization of sinking organic matter. Ocean circulation and physical processes continually drive
37 the large-scale distribution of chemicals (Williams and Follows, 2003) toward a homogeneous
38 distribution. Therefore, nutrient dynamics is important to understand the overall ecosystem productivity
39 and carbon cycles. In general, the surface layer is depleted in nutrients in low latitude regions (Sarmiento
40 and Toggweiler, 1984), but in some ocean regions, called high nutrient low chlorophyll (HNLC) regions,
41 nutrient concentrations tend to be anomalously high, particularly in areas of the North Atlantic and
42 Southern Ocean, as well as in the eastern equatorial Pacific, and in the North Pacific; see e.g. Pondaven
43 et al. (1999). In the Mediterranean, the surface layer is usually nutrient-depleted. Most studies show that
44 nitrate is the most common limiting factor for primary production in the global ocean (Moore et al.,
45 2013), while others evidence that phosphate may be a limiting factor in some specific areas, as is the
46 case of the Mediterranean Sea (Diaz et al., 2001; Krom et al., 2004).

47 Being an enclosed marginal sea, the Mediterranean Sea exhibits an anti-estuarine circulation,
48 responsible for its oligotrophic character (Bethoux et al., 1992; Krom et al., 2010) and acting like a
49 subtropical anticyclonic gyre. The Atlantic Water (AW), characterized by low-salinity and low-nutrient
50 content, enters the Western Mediterranean Sea (WMED) at the surface, through the Strait of Gibraltar,
51 and moves toward the Eastern Mediterranean Sea (EMED), crossing the Sicily Channel (Fig. 1). In the
52 Levantine and in the Cretan Sea, the AW becomes saltier, warmer and denser, and it sinks to
53 intermediate levels (200-500 m) to form the Intermediate Water (IW, Schroeder et al., 2017). The IW
54 (which may be further called Levantine or Cretan Intermediate Water, LIW or CIW) flows westward
55 across the entire Mediterranean Sea to the Atlantic Ocean (Fig. 1). As for the deep layer, the Western
56 Mediterranean Deep Water (WMDW or DW) is formed in the Gulf of Lion through deep convection
57 (Testor et al., 2018; MEDOC Group, 1970; Durrieu de Madron et al, 2013) while the Eastern
58 Mediterranean Deep Water (EMDW) is formed in the Adriatic Sea and occasionally in the Aegean Sea
59 (Lascaratos et al., 1999; Roether et al., 1996, 2007).

60



61 **Figure 1.** Map of the western Mediterranean Sea showing the main regions with a sketch of the AW,
 62 IW and DW major paths.

63 The Mediterranean Sea is known to be a hotspot for climate change (Giorgi, 2006; Cheng et al., 2021).
 64 During the early 1990s, the Deep Water (DW) formation area of the EMED shifted from the Adriatic
 65 Sea to the Aegean Sea. This event is known as the Eastern Mediterranean Transient (EMT; Roether et
 66 al., 1996, 2007, 2014; Roether and Schlitzer, 1991; Theocharis et al., 2002). As a consequence, the
 67 intermediate and deep waters of the EMED became saltier and warmer (Lascaratos et al., 1999;
 68 Malanotte-Rizzoli et al., 1999). The EMT affected the WMED as well, not only changing the
 69 thermohaline characteristics of the IW and concurring to the preconditioning of the Western
 70 Mediterranean Transition (WMT; Schroeder et al., 2016), which set the beginning of a rapid warming
 71 and salting of the deep layers in the WMED since 2005 (Schroeder et al., 2006; Schroeder et al., 2010,
 72 2016; Piñeiro et al., 2019). Over the last decade, it has been evidenced that heat and salt content have
 73 been increasing all over the deep western basin (Schroeder et al., 2016).

74 Changes in circulation due to an increased stratification limit the exchange of materials between the
 75 nutrient-rich deep layers and the surface layers. Understanding the peculiar oligotrophy of the
 76 Mediterranean Sea is still a challenge, since there is not an exact quantification of nutrient sinks and
 77 sources. Studies like Crispi et al. (2001), Ribera d'Alcalà (2003), Krom et al. (2010) and Lazzari et al.
 78 (2012) related the horizontal spatial patterns in nutrient concentrations mainly to the anti-estuarine
 79 circulation which exports nutrients to the Atlantic Ocean, showing a decreasing tendency of nutrient
 80 concentrations toward east, as opposed to the salinity horizontal gradient. Others related it to the
 81 influence of the atmospheric deposition (Bartoli et al., 2005; Béthoux et al., 2002; Huertas et al., 2012;
 82 Krom et al., 2010) and rivers discharges that are rich in nitrate and poor deficient in phosphate (Ludwig
 83 et al., 2009), which might explain the peculiarity in both EMED and WMED.

85 Lazzari et al. (2016) also argued that the variations in phosphate are regulated by atmospheric and river
86 inputs like Ebro and Rhône (Ludwig et al., 2009).

87 These variations, together with the anthropogenic perturbations affect the spatial distribution of nutrients
88 (Moon et al., 2016) while temporal variability is still unresolved.

89 De Fommervault et al. (2015) reported a decreasing phosphate and an increasing nitrate concentrations
90 trend between 1990 and 2010, based on a time series (DYFAMED) in the Ligurian Sea, while Moon et
91 al. (2016) evidenced an increase between 1990 and 2005 and a gradual decline after 2005 in both nitrate
92 and phosphate in the WMED and EMED.

93 At the global scale, most of the biogeochemical descriptions are based on model simulations and satellite
94 observations (using sea surface chlorophyll concentrations (Salgado-Hernanz et al., 2019)) but also on
95 the increasing use of Biogeochemical Argo floats (D'Ortenzio et al., 2020; Lavigne, 2015; Testor et al.,
96 2018), since in situ observations of nutrients are generally infrequent and scattered in space and time.
97 For this reason, climatological mapping is often applied to sparse in situ data in order to understand the
98 biogeochemical state of the ocean representing monthly, seasonally, or annually averaged fields.

99 Levitus (1982) was the first to generate objectively analyzed fields of potential temperature, salinity,
100 and dissolved oxygen, and to produce a climatological atlas of the world ocean.

101 Later on, the World Ocean Atlas (WOA), the North Sea climatologies and the Global ocean Carbon
102 Climatology resulting from GLODAP data product (Key et al., 2004, Olsen et al., 2020, Lauvset et al.
103 2021) used the Cressman analysis (1956) with modified Barnes scheme (Barnes 1964, 1994). In 1994,
104 the first World Ocean Atlas (WOA94; Conkright et al., 1994) was released integrating temperature,
105 salinity, oxygen, phosphate, nitrate, and silicate observations. Every four years there is a renewed release
106 of the WOA with an updated World Ocean database (WOD).

107 On the regional scale, the first salinity and temperature climatology of the Mediterranean Sea was
108 produced by Hecht et al. (1988) for the Levantine Basin. Picco (1990) was also among the first to
109 describe the WMED between 1909 and 1987. In 2002, the Medar/Medatlas group (Fichaut et al., 2003)
110 archived a large amount of biogeochemical and hydrographic in situ observations for the entire region
111 and used the Variational Inverse Model (VIM; Brasseur, 1991) to build seasonal and interannual gridded
112 fields. In 2006, the SeadataNet EU project integrated all existing data, to provide temperature and
113 salinity regional climatology products for the Mediterranean Sea using VIM as well (Simoncelli et al.,
114 2016), and dissolved inorganic nutrients (nitrate, phosphate and silicate) 6-years centered average from
115 1965 to 2017 are available on the EMODnet chemistry portal (<https://www.emodnet-chemistry.eu/>).
116 Within this context, in this study, regional climatological fields of in situ nitrate, phosphate and silicate,
117 using the Data Interpolation Variational Analysis (DIVAnd; Barth et al., 2014) are presented here,
118 providing a high-resolution field contributing to the existing products (Table 1).

119 The aim of this study is to give a synthetic view of the biogeochemical state of the WMED, to evaluate
120 the mean state of inorganic nutrients over 36 years of in situ observations and to investigate upon a
121 biogeochemical signature of the effect of the WMT .

122 The paper is organized as follows, section 2 describes the data sources used and the quality check;
123 section 3 is devoted to the methodology, section 4 presents the main results including a comparison of
124 the new climatology with other products. At the end, we address the change in biogeochemical
125 characteristics before and after WMT.

126 **Table 1.** Overview of the existing inorganic nutrient climatologies in the Western Mediterranean Sea.

Climatology	WOA	EMODnet	BGC-WMED (Present study)
Reference	(Garcia et al., 2019)	(Míguez et al., 2019)	(Belgacem et al., 2021)
Year of release	2018	2018	2021
Parameter	Nitrate/ Phosphate/ Silicate	Nitrate/ Phosphate/ Silicate	Nitrate/ Phosphate/ Silicate
Unit	$\mu\text{mol kg}^{-1}$	$\mu\text{mol L}^{-1}$	$\mu\text{mol kg}^{-1}$
Data type	CTD Bottle	CTD Bottle	CTD Bottle
Vertical resolution	Seasonal: 43 levels 0-800m Annual: 102 levels 0-5500m	21 standard depths 0-1100m (nitrate) 0-1500m (phosphate) 0-1500m (silicate)	19 levels 0-1500m
Horizontal resolution	1° latitude longitude grid	1/8°	1/4°
Observation time span	1955-2017	1970 to 2016 (nitrate) 1960 to 2016 (phosphate) 1965 to 2016 (silicate)	1981-2017
Area	Global	Mediterranean Sea	Western Mediterranean Sea
Temporal resolution	Season Decadal	Season 6 year running averages	whole observational period, and two sub-intervals (1981-2004, 2005-2017)
Climatology analysis method/ parameter	Objective analysis	DIVA (Data-Interpolating Variational Analysis) tool	DIVAnd (Data-Interpolating Variational Analysis N-dimension)
Correlation length	-	optimized and filtered vertically and a seasonally averaged profile was used.	optimized and filtered vertically and horizontally
Signal to noise ratio	-	A constant value = 1	A constant value = 0.5
Background field	-	the data mean value is subtracted from the data.	the data mean value is subtracted from the data
Detrending	-	No	No
Advection constraint applied	-	No	No

127

128 **2 Data**

129 The climatological analysis depends on the temporal and spatial distribution of the available in situ data,
130 and the reliability of these observations. Due to the scarcity of biogeochemical observations in the
131 WMED, merging and compiling data from different sources was necessary.

132 2.1 Data Sources

133 In total, 2253 in situ inorganic nutrient profiles are the base of the biogeochemical climatology of the
 134 WMED (Table 2) that is described here. These profiles cover the period 1981-2017 and come from the
 135 major data providers existing in the Mediterranean Sea, i.e. the Medar/MEDATLAS (1981-1996,
 136 Fichaut et al., 2003), the recently published CNR_DIN_WMED_20042017 biogeochemical dataset
 137 (2004-2017) (Belgacem et al., 2020), the MOOSE-GE cruises (Mediterranean Ocean Observing System
 138 for the Environment- Grande Échelle programme) (2011-2016, Testor et al., 2011, 2012, 2013, 2014,
 139 2015, 2016) stored in SeaDataNet data product (2001-2016) and EMODnet (the European Marine
 140 Observation and Data Network), GLODAPv2 (<https://www.glodap.info/>) and CARIMED
 141 (<http://hdl.handle.net/10508/11313>) data products and other data collected during MedSHIP programs
 142 (Schroeder et al., 2015) . All datasets are a selection of oceanographic cruises carried out within the
 143 framework of European projects such as the HYdrological cycle in the Mediterranean Experiment
 144 (HyMeX) Special Observing Period 2 (Estournel et al., 2016), the DEnse Water Experiment (DEWEX)
 145 project or by regional institutions having as objectives the investigation of the deep water convection
 146 and the biogeochemical properties of the of the WMED. Data were chosen to ensure high spatial
 147 coverage (Fig. 3).

148 **Table 2.** Number of inorganic nutrient profiles and data sources.

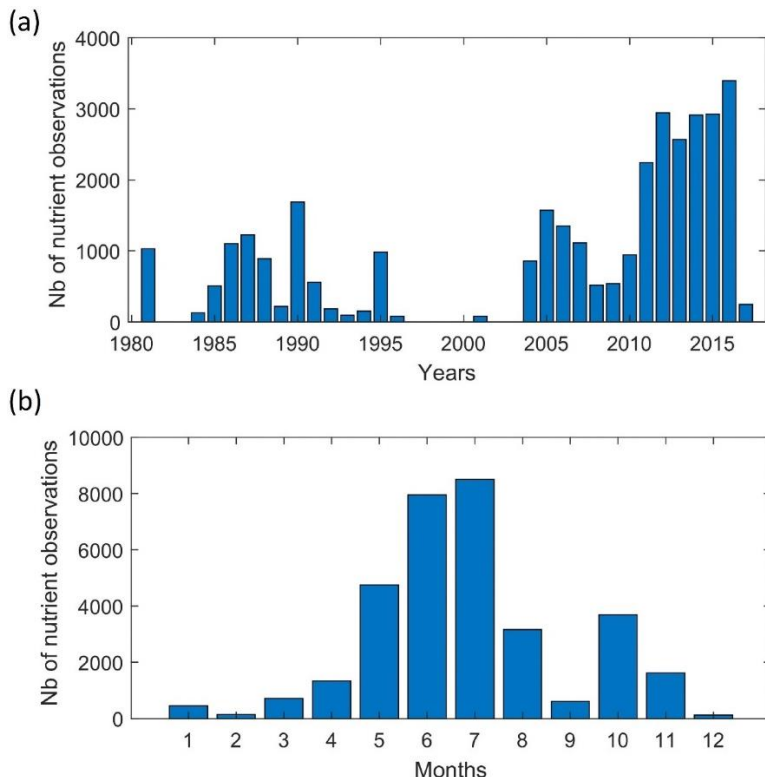
Source	N. of profiles	N. of observations	Link/ metadata
MEDATLAS	940	8839	http://www.ifremer.fr/medar/
SEADATANET including MOOSE-GE	523	15388	http://seadatanet.maris2.nl/v_rsm/content.asp?screen=0&history=yes https://doi.org/10.17600/11450160 https://doi.org/10.17600/12020030 https://doi.org/10.17600/13450110 https://doi.org/10.17600/14002300 https://doi.org/10.17600/15002500 https://doi.org/10.17600/16000700
CNR_DIN_WMED_20042017	737	8324	https://doi.org/10.1594/PANGAEA.904172
Other cruises	53	515	Medship programs; GLODAPv2; CARIMED (not yet available online, personal communication by Marta Álvarez) https://doi.org/10.1594/PANGAEA.902293
Σ	2253	33066	-

149

150 2.2 Data distribution

151 The data distribution per year is shown in Figure 2a. Most observations were collected between 1981
 152 and 1995, and between 2004 and 2017, with a marked gap between 1997 and 2003. Measurement
 153 distribution differs from month to month (Fig.2b) and tends to be biased towards the warm season. Very
 154 few measurements have been made during December-January-February, while June and July are the

155 months with the highest number of available observations (>7000). Consequently, the climatological
156 product may be considered as being more representative of spring and summer conditions.



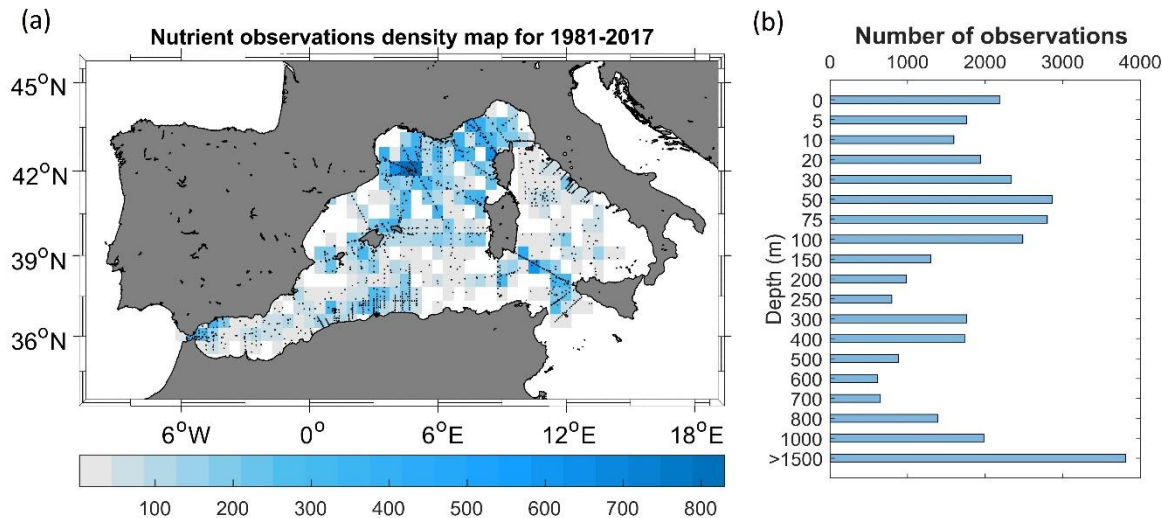
157

158 **Figure 2.** Temporal distribution of nutrient observations used for producing the BGC-WMED fields
159 (1981-2017), (a) yearly distribution and (b) monthly distribution.

160 Fig. 3a shows the regional distribution of nutrient measurements, while Fig. 3b indicates the number of
161 observations found in each depth range around the standard levels chosen for the vertical resolution of
162 the climatology.

163 Hydrological and biogeochemical measurements have always been repeatedly collected along several
164 repeated transects, known as key regions as the Sicily Channel and the Algéro-Provençal subbasin;
165 likewise, the northern WMED is a well sampled area, as it is an area of DW formation. Observation
166 density is still scarce (less than 100 observations) in some areas like the northern Tyrrhenian Sea.

167 The total number of measurements at each depth range underlines similar remarks, an uneven
168 distribution that needs to be considered in the selection of the vertical resolution to estimate the
169 climatological fields. Though, the use of 36 years of nutrient measurements to generate the
170 climatological fields significantly reduces the error field. In our case and taking into account the irregular
171 distribution in seasons and different years. A climatological gridded field was computed by analyzing
172 observations of three time periods regardless of the month: 1981-2017 and the subsets 1981-2004 and
173 2005-2017. We chose these subsets to investigate the effect of the WMT on nutrient distribution.



174

175 **Figure 3.** (a) Nutrient data density used for climatology analysis. Observations are binned in a regular
 176 1/2° × 1/2° latitude, longitude grid for each year over the period 1981-2017. Location of the stations
 177 included in the analysis are shown as black dots; (b) data distribution per depth range (i.e. at 800 m,
 178 observations between 800-1000 m are included).

179 **2.3 Data quality check**

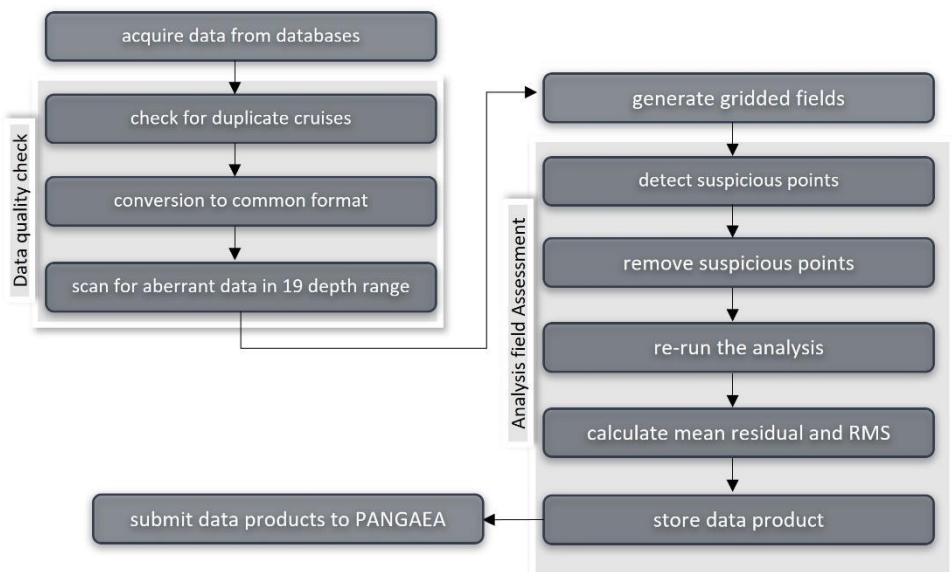
180 Data were gathered from different data sources, different analytical methods (Table A1.), thus before
 181 merging them, observations were first checked for duplicate (the number of profiles listed in Table 2
 182 refers to all data after removing duplicate measurements). The criteria to detect and remove duplicates
 183 is simple: observations collected during the same cruises extracted from the different sources were
 184 removed. Since profiles were measured during specific cruise (identified with a unique identification
 185 code) at specific time, data from duplicate cruises are removed.

186 Then, data was converted to a common format (similar to the csv CNR_DIN_WMED_20042017 data
 187 product, Belgacem et al., 2019). This recently released product contains measurements covering the
 188 WMED from 2004 to 2017. The data of the CNR_DIN_WMED_20042017 product have undergone a
 189 rigorous quality control process that was focused on a primary quality check of the precision of the data
 190 and a secondary quality control targeting the accuracy of the data, details about the adjustments and the
 191 applied corrections are found in Belgacem et al.(2020).

192 As detailed in Table 2, we combined observations from reliable sources (covering the time period 1981-
 193 2017), that were quality controlled according to international recommendations before being published
 194 (Maillard et al., 2007; SeaDataNet Group, 2010). Though, these historical data collections coming from
 195 sources different from the CNR_DIN_WMED_20042017 have been subjected to a quality check before
 196 merging them, to eliminate the effect of any aberrant observation. The check was carried out by
 197 computing median absolute deviations in 19 pressure classes (referring to the selected vertical resolution

198 of section 2.1, Fig.3b) (0-10, 10-30, 30-60, 60-80, 80-160, 160-260, 260-360, 360-460, 460-560, 560-
199 900, 900-1200, 1200-1400, 1400-1600, 1600-1800, 1800-2000, 2000-2200, 2200-2400, 2400-2600,
200 >2600 dbar). Any value that is more than three median absolute deviations from the median value is
201 considered a suspected measurement.

202 In total, 2.35% of nitrate observations, 2.44% of phosphate observations and 2.14% of silicate
203 observations were removed.



204

205 **Figure 4.** Flowchart describing the steps during the quality control; see text in section 2.3 and 3.3 for
206 more details.

207 3 Methods

208 3.1 Variational analysis mapping tool

209 Here, the **Data-Interpolating Variational Analysis- n dimension** (DIVAnd) method (Beckers et al., 2014;
210 Troupin et al., 2010, 2012) was used to generate the gridded fields. DIVA has been widely applied to
211 oceanographic climatologies, such as the SeaDataNet climatological products (Simoncelli et al., 2014,
212 2016, 2019, 2020a, 2020b, 2020c, 2021; Iona et al., 2018), EMODnet chemistry regional climatologies
213 (Míguez et al., 2019), the Adriatic Sea climatologies by Lipizer et al. (2014) or the black Sea (Capet et
214 al., 2014) and it was also applied to generate the global interior climatology GLODAPv2. 2016b
215 (Lauvset et al., 2016). It is an efficient mapping tool used to build a continuous spatial field from
216 discrete, scattered, irregular in situ data points with an error estimate at each level.

217 The BGC-WMED gridded fields have been computed with the more advanced N-dimensional version
218 of DIVA, DIVAnd v2.5.1 (Barth et al., 2014) (<https://doi.org/10.5281/zenodo.3627113>) using Julia as

219 a programming language (<https://julialang.org/>) under the Jupyter environment (<https://jupyter.org/>).
220 The code is freely available at <https://github.com/gher-ulg/DIVAnd.jl> (last access: January, 2020).

221 DIVA is based on the variational inverse method (VIM) (Brasseur et al., 1996). It takes into account the
222 errors associated with the measurements and takes account of the topography/bathymetry of the study
223 area. The method is designed to estimate an approximated field φ close to the observations and find the
224 field that minimizes the cost function $J[\varphi]$.

225 The cost function is defined as the misfit between the original data d_i , an array of N_d observations, the
226 analysis (observation constraint term) and a smoothness term. (Troupin et al., 2010):

$$227 J[\varphi] = \sum_{i=1}^{Nd} \mu_i Lc^2 (d_i - \varphi(x_i, y_i))^2 \quad (1) \text{ } Observation \text{ } constraint \text{ } term$$

$$228 + \int_D (\alpha_2 \nabla \nabla_\varphi : \nabla \nabla_\varphi + \alpha_1 Lc^2 \nabla_\varphi \cdot \nabla_\varphi + \alpha_0 Lc^4 \varphi^2) dD \quad (2) \text{ } Smoothness \text{ } term$$

229

230 Eq. (1)

231 where Lc is the correlation length, ∇ is the gradient operator, $\nabla \nabla_\varphi : \nabla \nabla_\varphi$ is the squared Laplacian of φ ,
232 the first term (observation constraint) considers the distance between the observations and the analysis
233 reconstructed field $\varphi(x_i, y_i)$, so that μ_i penalizes the analysis misfits relative to the observations. if the
234 observation constraint is only composed of $d_i - \varphi(x_i, y_i)$, the constructed field would be a simple
235 interpolation of the observations and the minimum is reached when $d_i = \varphi(x_i, y_i)$. The field $\varphi(x_i, y_i)$
236 need to be close to the observation and not have large variation. The second term (smoothness term)
237 measures the regularity of the domain of interest D . This expression within the integral remains
238 invariant (Brasseur and Haus, 1991). α_0 minimize the anomalies of the field itself, α_1 minimize the
239 spatial gradients, α_2 penalizes the field variability (regularization). The reconstructed fields are
240 determined at the elements of a grid on each isobath using the cost function Eq. (1).

241 The grid is dependent on the correlation length and the topographic contours of the specified grid in the
242 considered region, so there is no need to divide the region before interpolating.

243 The method computes two-, three- to four-multi-dimensional analyses (longitude, latitude, depth, time).
244 For climatological studies, the four-dimensional extension was used on successive horizontal layers at
245 different depths for the whole time period.

246 Along with the gridded fields, DIVA yields error fields dependent on the data coverage and the noise in
247 the measurements (Brankart and Brasseur, 1998; Rixen et al., 2000). Full details about the approach are

248 provided extensively by Barth et al. (2014) and Troupin et al. (2018) in the Diva User Guide
249 (<https://doi.org/10.5281/zenodo.836723>).

250 3.2 Interpolation parameters

251 DIVAnd is conditioned by topography, by the spatial correlation length (Lc) and by the signal-to-noise
252 ratio (SNR, λ) of the measurements, which are essential parameters to obtain meaningful results. They
253 are considered more in detail in the following sections.

254 3.2.1 Land-sea mask

255 A 3D dimension land-sea mask is created using the coastline and bathymetry of the General Bathymetric
256 Chart of the Oceans (GEBCO) 30-sec topography (Weatherall et al., 2015). The WMED is a relatively
257 small area which necessitates a high-resolution bathymetry to generate a mask at different depth layers.
258 The vertical resolution is set to 19 standard depth levels from the surface to 1500 m: 0, 5, 10, 20, 30, 50,
259 75, 100, 150, 200, 250, 300, 400, 500, 600, 700, 800, 1000, 1500 m, corresponding to the most
260 commonly used predefined levels for the sampling of seawater for nutrient analyses. The resulting fields
261 at each depth level are the interpolation on the specified grid. These depth surfaces are the domain on
262 which the interpolation is performed.

263 3.2.2 The spatial correlation length scale (Lc)

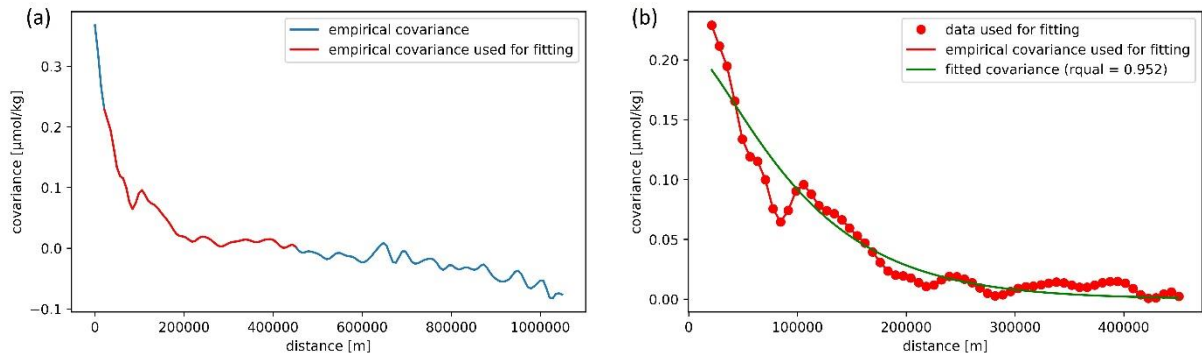
264 Lc indicates the distance over which an observation affects its neighbors. The correlation length can be
265 set by the user or computed using the data distribution.

266 For the BGC-WMED biogeochemical climatology, this parameter was optimized for the whole-time
267 span, and at each depth layer. The correlation length has been evaluated by fitting the empirical kernel
268 function to the correlation between data isotropy and homogeneity in correlations. The quality of the fit
269 is dependent on the number of observations (Troupin et al., 2018). The analytical covariance model used
270 in the fit is derived for an infinite domain (Barth et al, 2014). To assess the quality of the fit, the data
271 covariance and the fitted covariance are plotted against the distance between data points (Fig. 5). At 10
272 m, the correlation length was obtained with a high number of data points, indicating that the empirical
273 covariance used to estimate the covariance and the fitted covariance are in good agreement.

274 At some depth layers there are irregularities due to an insufficient amount of data points, making it
275 necessary to apply a smoothing filter/fit to minimize the effect of these irregularities. It has been tested
276 whether a randomly selected field analysis (nitrate data from 2006 and 2015) obtained with the fitted-
277 vertical correlation profile is better than the analysis with zero-vertical correlation. A skill score relative
278 to analysis non-fitted-vertical correlation has been computed following Murphy (1988) and Barth et al.
279 (2014):

280 $skill\ score = 1 - \frac{RMS_{no\ fit}^2}{RMS^2}$ Eq. (2)

281 A large difference in the global RMS between the analysis with the fitted-vertical correlation and the
 282 analysis with non-fitted-vertical correlation used for validation was found. The test shows whether the
 283 use of the fit in the correlation profile is improving the overall analysis or not. We found that the RMS
 284 error (nitrate analysis of 1981-2017) was reduced from $0.696\ \mu\text{mol kg}^{-1}$ (analysis without fit) to $0.571\ \mu\text{mol kg}^{-1}$
 285 (analysis with fit) at 10 m depth, which means using the fitted vertical correlation profile in
 286 the analysis improves the skill by 32 %, and the fit is improving the analysis fields.



287 **Figure 5.** Example of the Nitrate covariance. (a) The empirical data covariance function is given in red,
 288 the curve comes from the analysis of observations within depth = 10 m, while (b) the fitted covariance
 289 curve (theoretical kernel) is given in green.
 290

291 Based on the data, DIVA performs a least-square fit of the data covariance function with a theoretical
 292 function. Then, a vertical filter is applied and an average profile over the whole period is used (Fig. 6).
 293 This procedure is analogous to what has been used for the EMODnet climatology and the North Atlantic
 294 climatology, except that in EMODnet climatology, seasonally averaged profiles were used (Buga et al.,
 295 2019) and a monthly averaged profiles were used in North Atlantic climatology (Troupin et al., 2010).
 296 The filter is applied to discard aberration caused by outliers or scarce observations in some layers, as
 297 described above.

298 Because of the horizontal and vertical inhomogeneity of the data coverage, the analysis was based on a
 299 correlation length that varies both horizontally (Fig. 6a) and vertically (Fig. 6b).

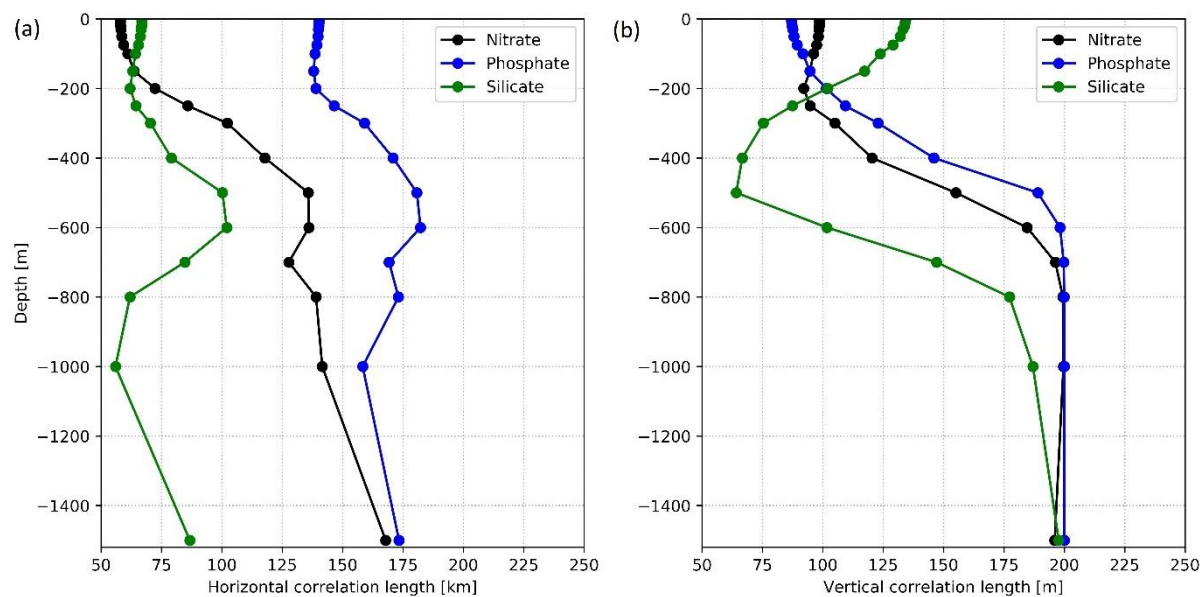
300 As expected, Lc increases with depth (Fig. 6), extending the influence area of the observation, a
 301 consequence of the fact that variability at depth is lower and that observations in the deep layer are
 302 scarcer (which on the other hand makes the Lc estimate more uncertain).

303 From the surface to 150-200 m, Lc is rather constant (Fig. 6), while from 200 to 600 m, the horizontal
 304 Lc (Fig. 6a) increases for all nutrients. Below 600 m, the horizontal Lc for silicate decreases down to
 305 1000 m, and then increases again at 1500 m. For nitrate and phosphate, a similar, but less marked,
 306 behavior is observed.

307 The vertical Lc (Fig. 6b) behaves similarly toward the increase, for nitrate and phosphate, due to the
 308 homogeneity of the intermediate water mass, as explained also by Troupin et al. (2010). For silicate, the
 309 vertical Lc decreases in the intermediate depth, reaching a minimum at 500 m depth. The different
 310 behavior of silicate could be explained by the progressive increase in concentrations from the surface to
 311 the deep layer, compared to nitrate and phosphate vertical distribution (strong gradient between surface
 312 depleted layer and intermediate layer). Lc for silicate has lower values compared to nitrate and
 313 phosphate, because, horizontally and vertically, it behaves in a different way. Unlike nitrate and
 314 phosphate, silicate does not show a strong east-west increased gradient. This gradient might induce this
 315 difference in the horizontal distance over which the sample influences its neighborhood.

316 Besides, silicate is less utilized by primary producers, and the dissolution of the biogenic silica is slower
 317 than that of the other nutrients (DeMaster, 2002) which explain its progressive increase towards deeper
 318 layers (Krom et al., 2014). The vertical Lc for all nutrients increases progressively from 400 m to 1500
 319 m.

320 Troupin et al. (2010) and Iona et al. (2018) attributed similar changes observed in Lc for temperature
 321 and salinity to the variability of the water masses in each layer. This might also explain the changes
 322 found in Lc for nutrients. Indeed, the concentration of nutrients in the WMED increases with depth and
 323 is very low at the surface, which explains the constant low values of Lc in this layer.



324
 325 **Figure 6.** (a) Horizontal and (b) vertical optimized correlation lengths, for each nutrient (1981-2017),
 326 as a function of depth.

327 3.2.3 Signal-to-Noise Ratio

328 The signal-to-noise ratio (SNR) is related to the confidence in the measurements. It is the ratio between
 329 the variance of the signal and the variance of the measurement noise/error. The SNR defines the

330 representativeness of the measurements relative to the climatological fields, in other words, it is the
331 confidence in the data.

332 It not only depends on the instrumental error but also on the fact that observations are instantaneous
333 measurements, and since a climatology is a long-term mean, such observations do not represent exactly
334 the same.

335 Generally, small SNR values favor large deviations from the real measurements to give a smoother
336 climatological field. On the other hand, with a high SNR, DIVAnd keeps the existing observations and
337 interpolates between data points. The need is to find an approximation that does not deviate much from
338 the real observations (further details in Lauvset et al., 2016, and Troupin et al., 2010).

339 Following the same approach that many climatologies that used the DIVAnd method adopted, i.e.
340 EMODnet climatologies (available on the EMODnet chemistry portal), the Atlantic regional
341 climatologies (Troupin et al., 2010), the Adriatic Sea climatology (Lipizer et al., 2014) and the
342 SeadataNet regional climatology (Simoncelli et al., 2015), the SNR is set to a constant value (Table 1).

343 The analysis is performed with a predefined uniform default error variance of 0.5 for all parameters at
344 all depths, we presume that the data sources used to generate BGC-WMED climatology are consistent
345 products. Three iterations are done inside DIVAnd to estimate the optimal scale factor of error variance
346 of the observation (following Desroziers et al., 2005). More details can be found in <https://gher-ulg.github.io/DIVAnd.jl/latest/#DIVAnd.diva3d>.

348 Values of SNR provided by means of a generalized cross-validation (GCV) technique (Brankart and
349 Brasseur, 1998) gave a large estimate of the SNR (of the order of 22) showing a discontinuous analysis
350 field and patterns around the cruise transects that do not represent properly the climatological fields.

351 3.3 Detection of suspicious data

352 Assessment of the analysis is performed by detecting outliers and suspicious data , in order to remove
353 observations that generate irregular interpolated fields; and suspect observations that were not detected
354 in the data quality check of section 2.3.

355 The automatic check measures how consistent the gridded field is, with respect to the nearby
356 observations, by estimating the difference between a measurement and its analysis scaled by the
357 expected error; based on that, a score is assigned to each observation. Data points with the highest scores
358 were considered as suspect and were removed from the analysis (Fig. A1, A2, A3). Overall, 0.031%,
359 0.014%, 0.004% data points, for nitrate, phosphate, and silicate, respectively, were considered
360 inconsistent. Details about the quality check values and range are plotted in the appendix (Table A1).

361 3.4 Quality check of the analysis fields

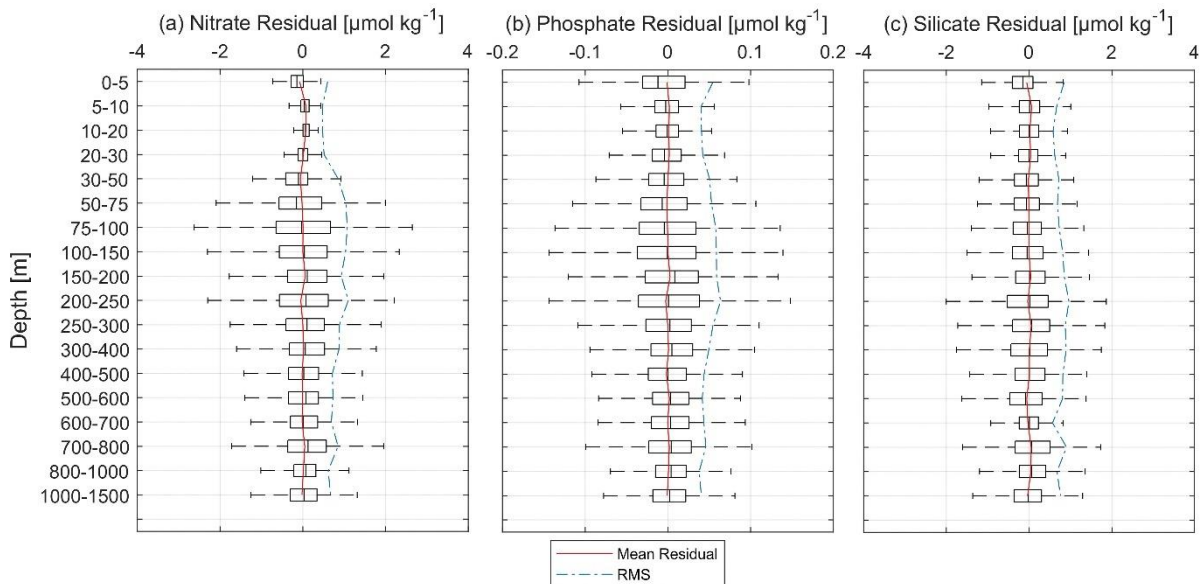
362 The quality of the climatology was checked against observations by estimating the mean residual and
363 the root mean squared (RMS) of the difference between the climatology and the observations. Averages
364 over the entire basin were calculated between depth surfaces (see section 2.3). Residuals are the
365 difference between the observations within the specific depth surface and the analysis (interpolated
366 linearly to the location of the observations) and are estimated by depth range (Fig. 7). The analysis fields
367 at each depth range (i.e. depth surfaces or domain on which the interpolation is performed) are the
368 interpolation on the specified grid. In Fig. 7, we present the vertical profile of the mean residuals and
369 RMS at different depth ranges for the three nutrients.

370 Nitrate observations and the analysis field in Fig.7a have a high level of agreement in the surface layer
371 (from 0 to 30 m depth). Just below (between 30 and 200 m), boxplots are suggestive of larger differences.
372 From surface to the deep layer, the mean residual between nitrate observation and the gridded field
373 varied between -0.075 and 0.0765 $\mu\text{mol kg}^{-1}$, while the corresponding RMS fluctuated between 0.47 and
374 1.1 $\mu\text{mol kg}^{-1}$. This is justified by the inhomogeneity of the observations mainly in deep layers.

375 As for the average residual between phosphate observations and the gridded analysis (Fig.7b), it was
376 around zero and varied between -0.0027 and 0.0026 $\mu\text{mol kg}^{-1}$. The RMS for phosphate was between
377 0.037 and 0.063 $\mu\text{mol kg}^{-1}$.

378 Silicate residuals (Fig. 7c), on the other hand, seemed more homogeneous at all depth levels. The highest
379 level of agreement was found below 20 m and at 600 m. Overall, residuals varied between -0.057 and
380 0.063 $\mu\text{mol kg}^{-1}$, while the RMS ranged between 0.567 and 0.963 $\mu\text{mol kg}^{-1}$.

381 Over the entire water column, the mean residual was around zero (0.004 $\mu\text{mol kg}^{-1}$ for nitrate, 0.0002
382 $\mu\text{mol kg}^{-1}$ for phosphate and 0.003 $\mu\text{mol kg}^{-1}$ for silicate) (Fig. 7). The RMS (in blue line) fell within the
383 mean residual +/- standard deviation in the upper 25th percentile at the different depth ranges and in all
384 parameters meaning that in general, the bias between the observations and the analysis is small and there
385 is a good agreement.



386

387 **Figure 7.** Vertical mean residuals (in red), i.e. the differences between the observations and the analysis,
 388 and the mean RMS (dashed blue) of (a) nitrate, (b) phosphate, (c) silicate.

389 **4 Results**

390 The final result consists of gridded fields of mapped climatological means of inorganic nutrients for the
 391 periods 1981-2004, 2005-2017, and the whole period 1981-2017, produced with VIM described in
 392 section 3, using data of section 2. Together with the gridded fields, error maps have been generated to
 393 check the degree of reliability of the analysis.

394 The resulting climatologies (Table 3) are aggregated in a 4D netCDF for each nutrient and each time
 395 period that contains the interpolated field of the variable and the related information: associated relative
 396 error, variable fields masked using two relative error thresholds (L1 and L2). The mapped climatology
 397 is available from PANGAEA (<https://doi.pangaea.de/10.1594/PANGAEA.930447>, Belgacem et al.,
 398 2021) as one folder named BGC-WMED climatology. This folder contains nine files: three per
 399 parameter and three per time period.

400 Here is an example of the analysis output found in the netCDF. Figure 8 shows the unmasked
 401 climatological field of the mean spatial variation of nitrate, relative error field distribution, the masked
 402 climatological field using relative error with two threshold values (0.3 and 0.5) to assess the quality of
 403 the resulting fields.

404

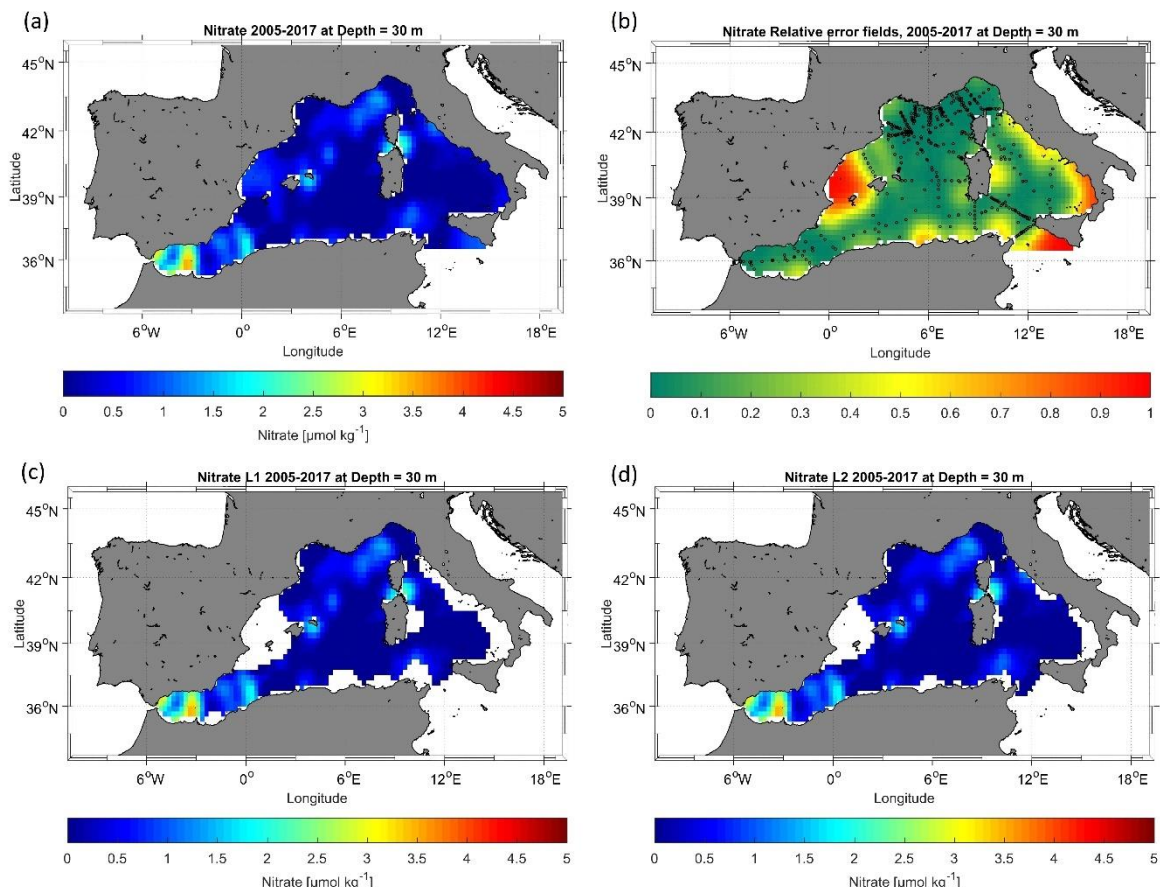
405

406

407 **Table 3.** Available analyzed fields and related information in the netCDF files.

Variable name	Field name	Description
Lon	Longitude	Longitude in degrees east, extent: $-7 - 17.25^{\circ}\text{E}$
Lat	Latitude	Latitude in degrees north, extent: $33.5 - 45.85^{\circ}\text{N}$
depth	Depth	Depth in meters, 19 levels, range: $0 - 1500\text{ m}$
nitrate/phosphate/silicate	DIVAnd analyzed climatology	Mapped climatological fields
nitrate_L1/phosphate_L1/	Nitrate/Phosphate/Silicate	Mapped climatological fields masked using
silicate_L1	masked field level 1	relative error threshold 0.3.
nitrate_L2/ phosphate_L2/	Nitrate/Phosphate/Silicate	Mapped climatological fields masked using
silicate_L2	masked field level 2	relative error threshold 0.5.
nitrate_relerr/phosphate_re	Nitrate/Phosphate/Silicate	Mapped relative error fields associated to the
lerr/silicate _relerr	masked relative error	climatological field

408



409

410 **Figure 8.** Example of nitrate analysis for the period 2005-2017 (a) unmasked analysis field, (b) relative
411 error field distribution with the observation in black circles, (c) masked analysis fields masked using
412 relative error threshold = 0.3, and (d) masked analysis fields masked using relative error threshold = 0.5.

413 4.1 Nutrient climatological distribution

414 A description of the spatial patterns of the dissolved inorganic nutrients across the domain and over the
415 entire period (1981-2017) is given. The gridded fields for nitrate, phosphate, and silicate are discussed
416 at three depth levels, representative of the surface (at 100 m), intermediate (at 300 m), and deep layer

417 (at 1500 m). The horizontal maps at the selected depths are shown in Fig. 9, while the average vertical
418 profiles of nutrients over the whole area are shown in Fig. 10.

419 4.1.1 Surface layer

420 The nitrate, phosphate and silicate mean climatological fields over 1981-2017 are presented in Fig. 9 (a,
421 b, c) respectively. The mean surface nitrate at 100 m is about $3.58 \pm 1.16 \mu\text{mol kg}^{-1}$. Highest surface
422 values of nitrate concentrations are found in regions where strong upwelling or vertical mixing occurs,
423 such as the Liguro-Provençal basin and the Alboran Sea (see Fig. 9a), and regions with extensive supply
424 by the Ebro, Rhone, Moulouya and Chelif rivers.

425 The convection region (Gulf of Lion and Ligurian Sea) is characterized by an eutrophic regime and a
426 spring bloom (Lavigne et al., 2015), unlike the rest of the basin that shows low nitrate concentrations in
427 the surface layer ($< 4 \mu\text{mol kg}^{-1}$).

428 Nutrient patterns in the Alboran Sea have been associated with the distinct vertical mixing that supplies
429 the surface layer with nutrients (Lazzari et al., 2012; Reale et al., 2020).

430 Indeed, the northern Alboran Sea is known as an upwelling area, where permanent strong winds enhance
431 the regional biological productivity (Reul et al., 2005). Nitrate distribution at 100 m presents a clear
432 distinction between the enriched surface regions in the WMED, under the influence of deep convection
433 processes, and the easternmost depleted regions.

434 The distribution of phosphate concentration has striking similarities with that of nitrate (Fig. 9b). The
435 mean surface phosphate concentration at 100 m, is $0.16 \pm 0.06 \mu\text{mol kg}^{-1}$. As for nitrate, the highest
436 surface values are found in the Alboran Sea, Balearic Sea, Gulf of Lion and Liguro-Provençal Basin
437 ($0.2\text{--}0.3 \mu\text{mol kg}^{-1}$), while the Tyrrhenian Sea and the Algerian Sea revealed phosphate concentrations
438 that were $<0.2 \mu\text{mol kg}^{-1}$. Similar patterns were observed by Lazzari et al. (2016), who argued that the
439 variations in phosphate are regulated by atmospheric and terrestrial inputs. It should be noted that the
440 maximum in the surface is found near river discharges of freshwater, like Ebro and Rhône, i.e. the largest
441 rivers of the WMED (Ludwig et al., 2009).

442 Concerning the distribution of silicate concentration, the surface layer at 100 m (Fig. 9c) followed the
443 same pattern as nitrate and phosphate. Over this layer the mean silicate was about $2.7 \pm 0.7 \mu\text{mol kg}^{-1}$.
444 As for nitrate and phosphate, the highest values ($3\text{--}4 \mu\text{mol kg}^{-1}$) were recorded in the Alboran Sea,
445 Balearic Sea, Gulf of Lion and Liguro-Provençal Basin and in the southern entrance of the Tyrrhenian
446 Sea. This surface distribution is in good agreement with the findings of Crombet et al. (2011), relating
447 this local silicate surface maximum to the continental input, river discharge and atmospheric deposition
448 (Frings et al., 2016; Sospedra et al., 2018). The spatial minima were reported in the Tyrrhenian Sea and
449 in the Algerian Sea ($<3 \mu\text{mol kg}^{-1}$).

450 4.1.2 Deep and Intermediate layer

451 At the basin scale, nitrate concentrations increase with depth (Fig. 10a), with the highest concentration
452 found at intermediate levels (250-500 m), ranging between 8.8 and 9.0 $\mu\text{mol kg}^{-1}$. In this 300 m layer
453 (Fig. 9d), nitrate concentration average is $7.2 \pm 1.06 \mu\text{mol kg}^{-1}$. High values ($> 6.5 \mu\text{mol kg}^{-1}$) are found
454 in the westernmost regions (Alboran Sea, Algerian Sea, Gulf of Lion, Balearic Sea and the Liguro-
455 Provençal Basin), while the easternmost regions (Tyrrhenian Sea, Sicily Channel), exhibit much lower
456 concentrations (between 4.5 and 6.5 $\mu\text{mol kg}^{-1}$).

457 Similar features are observed in the deep layer, at 1500 m (Fig. 9a), with nitrate concentrations
458 increasing all over the basin, reaching on average 7.8 - 7.9 $\mu\text{mol kg}^{-1}$ between 1000 and 1500 m depth
459 (Fig. 10a).

460 In both layers (300 m and 1500 m), the difference between the eastern opening of the basin (Sicily
461 Channel) and the western side (Alboran Sea) is noticeable: the Sicily Channel and the Tyrrhenian Sea
462 are under the direct influence of the water masses coming from the oligotrophic EMED, which then
463 gradually become enriched with nutrients along its path, as found by Schroeder et al. (2020).

464 Phosphate concentrations at intermediate depth (see 300 m, Fig. 9e), varied between 0.12 and 0.44 μmol
465 kg^{-1} , and the horizontal map shows the same gradual decrease towards east, with the highest
466 concentrations in the westernmost regions and minimum values in the eastern regions ($< 0.25 \mu\text{mol kg}^{-1}$).
467

468 The average vertical profile over the entire region (Fig. 10b), reveals a maximum in phosphate
469 concentrations between 300 and 800 m depth, related to an increased remineralization process.

470 In the deep layer (see 1500 m, Fig. 9h), phosphate concentration average is $0.36 \pm 0.02 \mu\text{mol kg}^{-1}$.
471 Generally, the deep layer is homogeneous (Fig. 10b). The difference observed between westernmost
472 regions and the Tyrrhenian Sea remains, though the latter demonstrate higher phosphate concentrations
473 ($\sim 0.3 \mu\text{mol kg}^{-1}$). This variation could be due to the difference in the water masses. The IW inflow from
474 the EMED brings relatively young waters that are depleted in nutrients, while the higher concentrations
475 in the deep layer are signatures of the older resident DW of the Tyrrhenian Sea. The change in the
476 biological uptake in the intermediate source water could explain the regional variability of nutrients.
477 The low productivity (D'Ortenzio and Ribera d'Alcalà, 2009) and the pronounced oligotrophic regime
478 of EMED water (Lazzari et al., 2016) may justify the increase in nutrients in the IW.

479 Silicate concentration distribution at intermediate (300 m, Fig. 9f) and deep layers (1500 m, Fig. 9i),
480 were as expected, showing a notable increase, compared to the surface. Here, the silicate average
481 concentration is $5.83 \pm 0.66 \mu\text{mol kg}^{-1}$. The maximum values were observed below 800 m, $> 8.034 \mu\text{mol}$
482 kg^{-1} (Fig. 10c). At 1500 m, silicate distribution is homogeneous all over the basin (on average $8.35 \pm$
483 0.39).

484 Generally, primary producers do not require silicate for their growth as much as they need nitrate and
485 phosphate which explain the disparity between nutrients patterns. Furthermore, at intermediate levels,

486 the water is warmer than at deep levels, enhancing the dissolution rate and the progressive increase in
487 silicate (DeMaster, 2002). The biogenic silicate is exported to greater depths and continues to dissolve
488 generating inorganic silicate as it sinks to the bottom. The recycling of silicate within the deep-sea
489 sediments is later on redistributed by the deep currents which explain the homogenous horizontal
490 distribution over the entire basin.

491 Comparing the three nutrients at the same depth levels, at the surface (100 m), it appears that they all
492 show local surface maximum, depending on local events such as strong winds, local river discharge and
493 vertical mixing (Ludwig et al., 2010).

494 In the easternmost areas, the surface depletion in nutrients (Van Cappellen et al., 2014) is attributed to
495 the variation in the thermohaline properties that has impacted primary production (Ozer et al., 2017) and
496 the export of organic matter to intermediate and deep layers leading to the accumulation of nutrients in
497 these depth ranges.

498 The Tyrrhenian Sea is not directly connected to convection regions. Here, the EMED water inflow plays
499 a major role. Li and Tanhua (2020) found an increased ventilation of the intermediate and deep layers
500 during 2001 to 2018 in the Sicily channel and a constant AOU between 2001-2016, suggesting a constant
501 ventilation that explains the peculiar nutrient distribution in that area. In the western side of the WMED,
502 intermediate and deep layers exhibit an increase in nutrients. Schroeder et al. (2020) explained this
503 increase in nitrate and phosphate at the intermediate layer with the increase of the remineralization rate
504 at these depths along the path of IW.

505 The deficiency of inorganic nutrients is explained by the effect of the anti-estuarine circulation, with the
506 IW coming from the EMED, which is known to be poor in nutrients (Krom et al., 2014; Schroeder et
507 al., 2020), accumulates nutrients along its path. Thus, this relative nutrient-rich Mediterranean outflow
508 is lost to the Atlantic Ocean.

509 Overall, in surface layer, circulation, physical processes, and vertical mixing increase nutrient input
510 while the biological pump controls the decrease.

511 In the deep layer, the variability is lower (standard deviation is reduced toward the bottom for all three
512 nutrients, see Fig.10), the deep layer accumulates dissolved organic nutrients. In the WMED, the deep
513 layer constitutes a reservoir of inorganic nutrients.

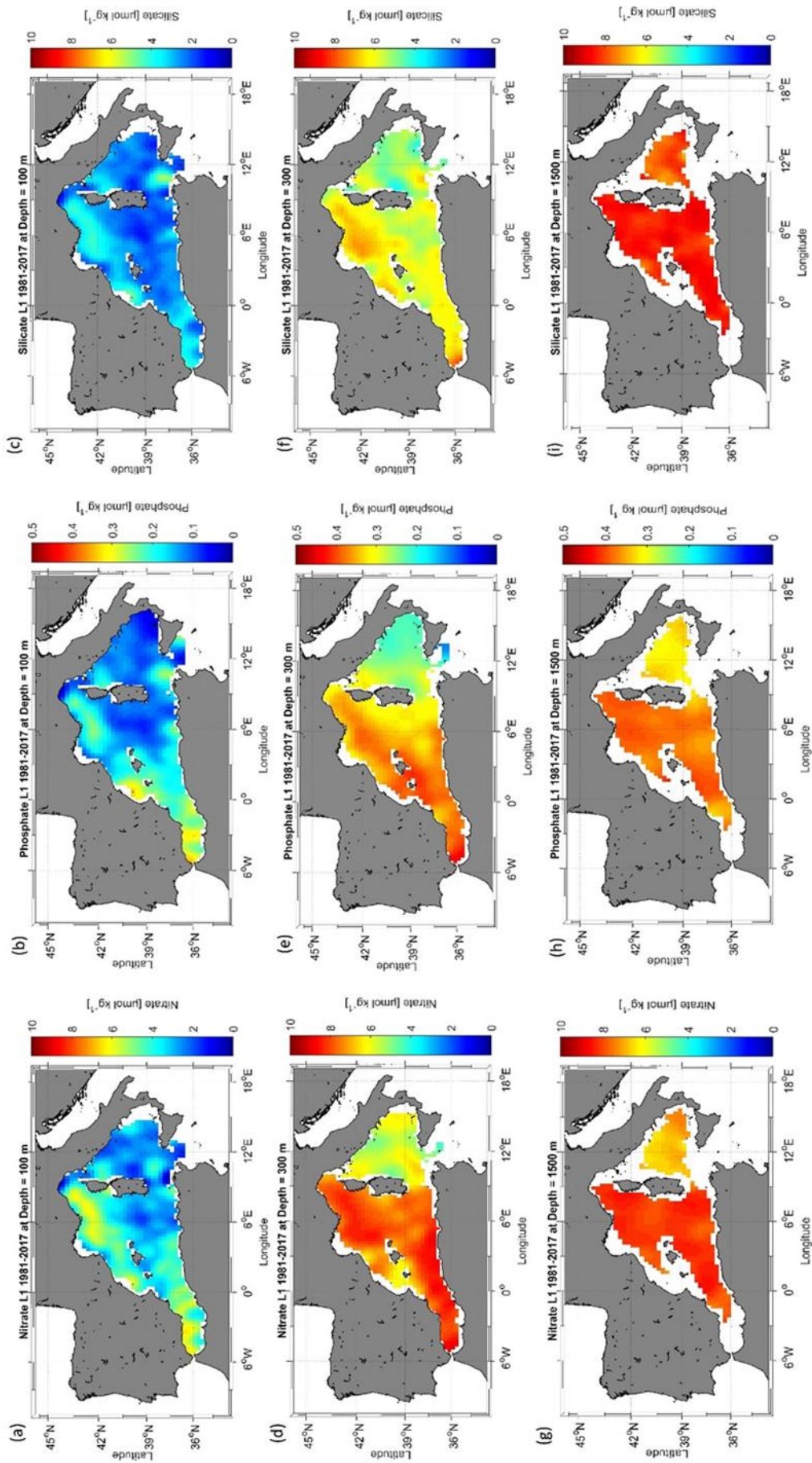
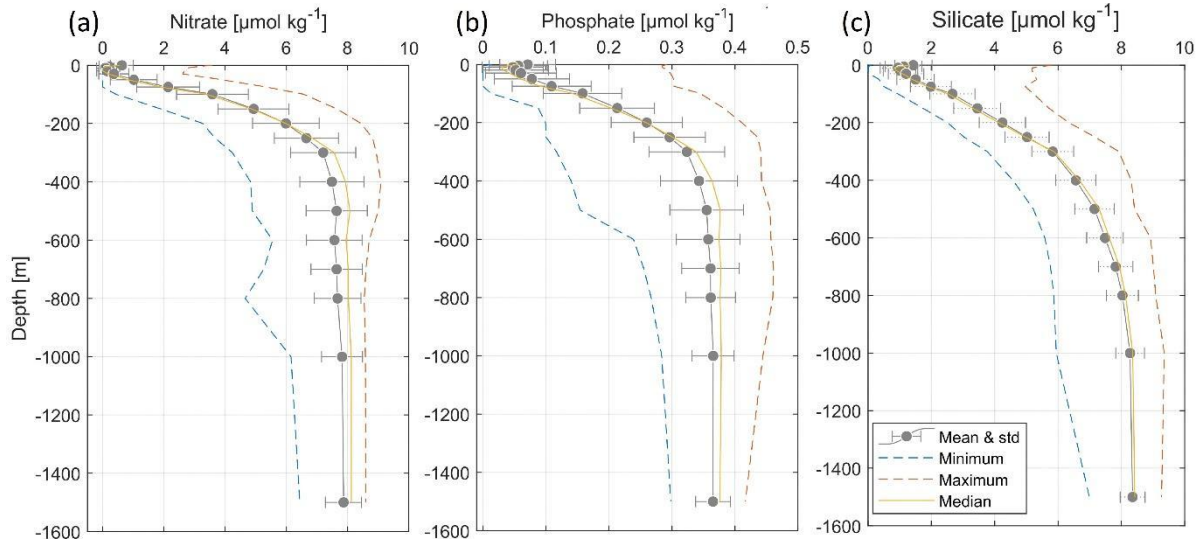


Figure 9. Climatological map distribution of nitrate (a. at 100 m, d. at 300 m, g. at 1500 m), phosphate (b. at 100 m, e. at 300 m, h. at 1500 m) and silicate (c. at 100 m, f. at 300 m, i. at 1500 m) for the period from 1981 to 2017.



514

515 **Figure 10.** Climatological mean vertical profiles of (a) nitrate, (b) phosphate and (c) silicate
 516 concentrations in the WMED (1981-2017). Dashed blue line indicates the minimum, dashed orange line
 517 indicates the maximum, continuous yellow line indicates median profile, error bars and mean profile are
 518 in grey.

519 **4.2 Error fields**

520 The determination of the error field is important to gain insight in the confidence in the climatological
 521 results. Mostly, the error estimate depends on the spatial distribution of the observations and the
 522 measurement noise. In DIVAnd, there are different methods available to estimate the relative error
 523 associated with the analysis fields.

524 A climatological field is computed at several depths (19 levels in this case), for different parameters
 525 (nitrate, phosphate, and silicate in this case). Given these premises and following the approach of similar
 526 climatologies (GLODAPv2.2016b, Lauvset et al., 2016; SeaDataNet aggregated data sets products,
 527 Simoncelli et al., 2015), for the BCG-WMED the error fields were estimated using the default DIVAnd
 528 method, i.e. the “clever poor man's error approach”, a less time consuming but efficient computational
 529 approach. According to Beckers et al. (2014) who also provides details about the mathematical
 530 background of the error fields computation, this method appropriately represents the true error and
 531 provides a qualitative distribution of the error estimate. This estimate is used to generate a mask over
 532 the analysis fields. Two error thresholds were applied (0.3 (L1) and 0.5 (L2)). Fig.8b., show the main
 533 error that occurs in regions void from measurements. An example of the analysis masked with the error
 534 thresholds output is shown in Fig.8c (L1) and Fig.8d (L2). The associated error fields with the analysis
 535 fields are integrated in the data product.

536 4.3 Comparison with other biogeochemical data products

537 In this section, a comparison of the BGC-WMED product with the most known global and/or regional
538 climatologies, that are frequently used as reference products for initializing numerical models, is made.

539 Specifically, the analyzed fields are compared to the reference data products WOA18 (Garcia et al.,
540 2019), a large scale illustration of nutrient distribution computed by objective analysis using the World
541 Ocean Database 2018 (Boyer et al., 2018). The new product is also compared to the reanalysis of the
542 Mediterranean Sea biogeochemistry, medBFM, a CMEMS product that assimilates satellite and Argo
543 data and includes terrestrial inputs of nitrate and phosphate from 39 rivers (Teruzzi et al., 2019).

544 Since the products used for inter-comparison were not originated from the same interpolation method,
545 not for the same time period and with different spatial resolution, here the comparison is mostly targeted
546 on the general patterns of nutrients in the region.

547 Comparisons are carried out between horizontal maps (Fig.11-12-13), as well as along a vertical
548 longitudinal transect (Fig.16-17-18). In addition, following Reale et al. (2020), the first 150 m have been
549 evaluated (Fig.14-15), since this is a depth level with a representative amount of in situ observations in
550 all three products. The evaluation is based on the estimation of horizontal average, on BGC-WMED
551 climatology, the medBFM biogeochemical reanalysis and the WOA18 climatology by subregion. i.e. a
552 spatial subdivision made according to Manca et al. (2004).

553 Products have a different grid resolution, thus to compare them and combine variables on a compatible
554 grid, the BGC-WMED new climatological data product (at $0.25^\circ \times 0.25^\circ$) for the periods 1981-2017,
555 2005- 2017 and the medBFM biogeochemical reanalysis (at $0.063^\circ \times 0.063^\circ$) (Teruzzi et al. 2019)
556 (https://doi.org/10.25423/MEDSEA_REANALYSIS_BIO_006_008) for the period 2005- 2017, are
557 regridded on the WOA18 ($1^\circ \times 1^\circ$) grid , changing the resolution, of the existing grid to facilitate the
558 comparison of the transect from each product.

559 The regridding is computed at all depth levels of the different products using nearest neighbor
560 interpolation. Prior to the interpolation, the medBFM reanalysis of nitrate and phosphate have been
561 averaged across the period 2005-2017.

562 We then calculated spatial maps of the mean difference at 150 m between the new climatology and the
563 reference products and then an average across subregions was performed.

564 4.3.1 Comparison with WOA18 at 150 m

565 Fig. 11-12-13 show the analysis at the 150 m depth surface for the three nutrients. The BGC-WMED
566 (1981-2017) product reveals detailed aspects of the general features of nitrate (Fig. 11.a), phosphate
567 (Fig. 12a) and silicate (Fig.13a).

568 For the three nutrients, the new product reproduces patterns similar to the WOA18 all over the region.
569 It shows well-defined fields and higher values of nitrate and phosphate concentrations. In the new
570 product, nitrate concentrations varied between $2.31 - 7.3 \mu\text{mol kg}^{-1}$ the WOA18 values were $2.19 - 5.99$
571 $\mu\text{mol kg}^{-1}$.Phosphate ranges were similar between the two products between $(0.092- 0.35 \mu\text{mol kg}^{-1}$
572 (BGC-WMED) and $0.095 - 0.35 \mu\text{mol kg}^{-1}$ (WOA18)). Likewise, Silicate range values at 150 m were
573 not different ($2.07 - 4.99$ (BGC-WMED) and $1.57 - 5.75 \mu\text{mol kg}^{-1}$ (WOA18)).

574 The average RMS difference (RMSD) calculated from the difference between the WOA18 and BGC-
575 WMED all over the region at 150 m is about $1.14 \mu\text{mol kg}^{-1}$ nitrate (Fig. 11c), $0.055 \mu\text{mol kg}^{-1}$ for
576 phosphate (Fig. 12c) and $0.91 \mu\text{mol kg}^{-1}$ for silicate (Fig. 13c). Overall, the RMS error values were low
577 indicating limited disparity between the two products.

578 The difference field for every grid point reflects this discrepancy and shows areas with limited
579 agreement between the two products that can have a difference $>2 \mu\text{mol kg}^{-1}$ for nitrate (Fig. 11c), >0.1
580 $\mu\text{mol kg}^{-1}$ for phosphate (Fig. 12c), $>1.5 \mu\text{mol kg}^{-1}$ for silicate (Fig. 13c). This dissimilarity is also noted
581 with the low r^2 (Fig. 14) ($0.34, 0.20, 0.095$ for nitrate, phosphate, and silicate respectively)

582 The distribution of the surface nitrate concentrations (at 150 m) (Fig. 11a) of the new product is similar
583 to that shown in WOA18 (Fig. 11b). The largest difference between the two products occurs in northwest
584 areas and in the Alboran Sea (Fig. 11c), areas of higher concentrations, a more nutrient rich surface
585 water as described in section 4.1. The difference is pronounced in these regions likely because of the
586 occurrence of upwellings along the African coast and seasonal vertical mixing in the northern WMED,
587 contributing to the upload of nutrients to the surface which could explain the high nitrate and phosphate
588 concentration in the BGC-WMED. The WOA18 maps show weaker values of nutrient concentrations
589 compared to the new product which does not mean that there are fewer physical drivers, but it might
590 indicate that the new product holds more in situ observations than the WOA18 in the WMED.

591 Phosphate surface concentrations (Fig. 12) show similar differences as nitrate. The largest difference
592 with the surface phosphate of the WOA18 is found in the Alboran Sea, Northern WMED and Sicily
593 region (Fig. 12c).

594 As for silicate, the surface distribution shows large differences (Fig. 13c). The highest values are
595 observed in the northwest area of the new product, and in the Alboran Sea in the WOA18 climatology ,
596 this again accounts for the data coverage difference.

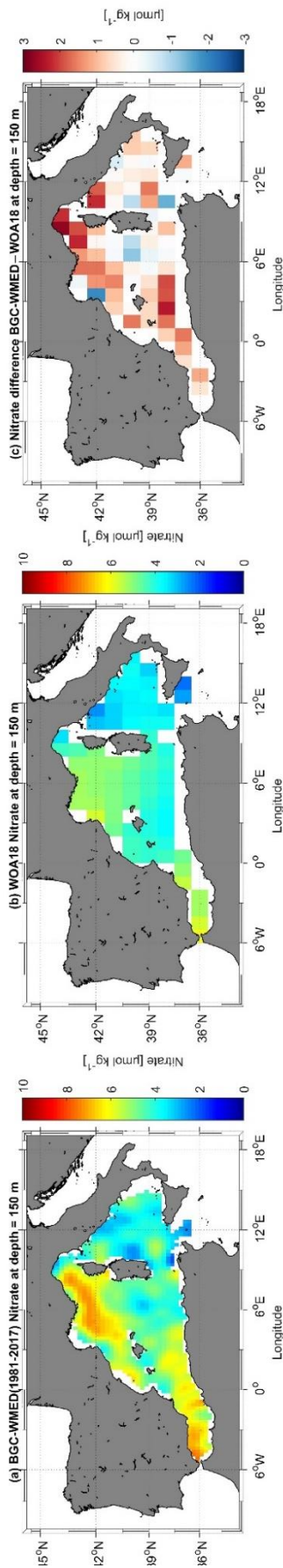


Figure 11. (a) BGC-WMED (1981-2017) Nitrate climatological field at 150 m depth; (b) WOA18 nitrate climatological field at 150 m depth; (c) difference between BGC-WMED and WOA18 nitrate fields at 150 m.

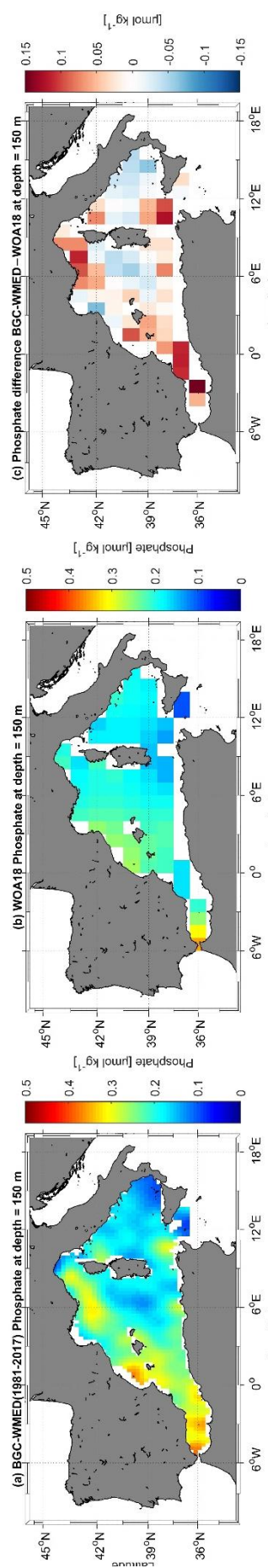


Figure 12. The same as Fig. 11 but for Phosphate.

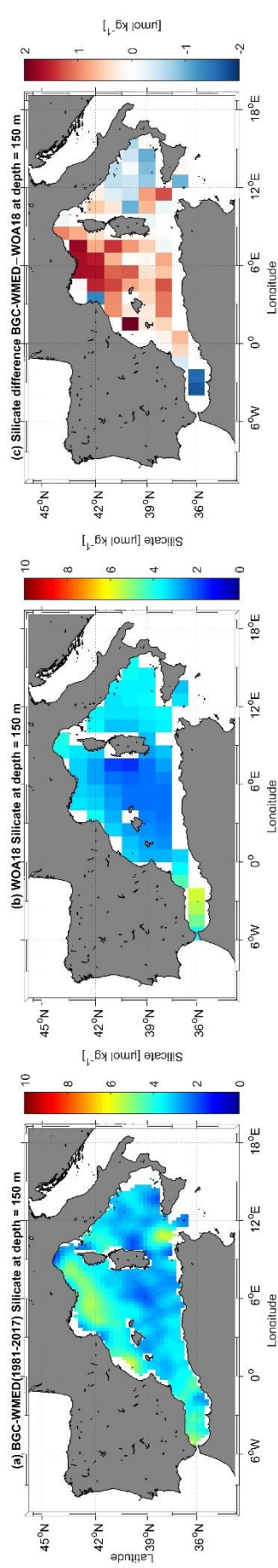


Figure 13. The same as Fig. 11 but for Silicate.

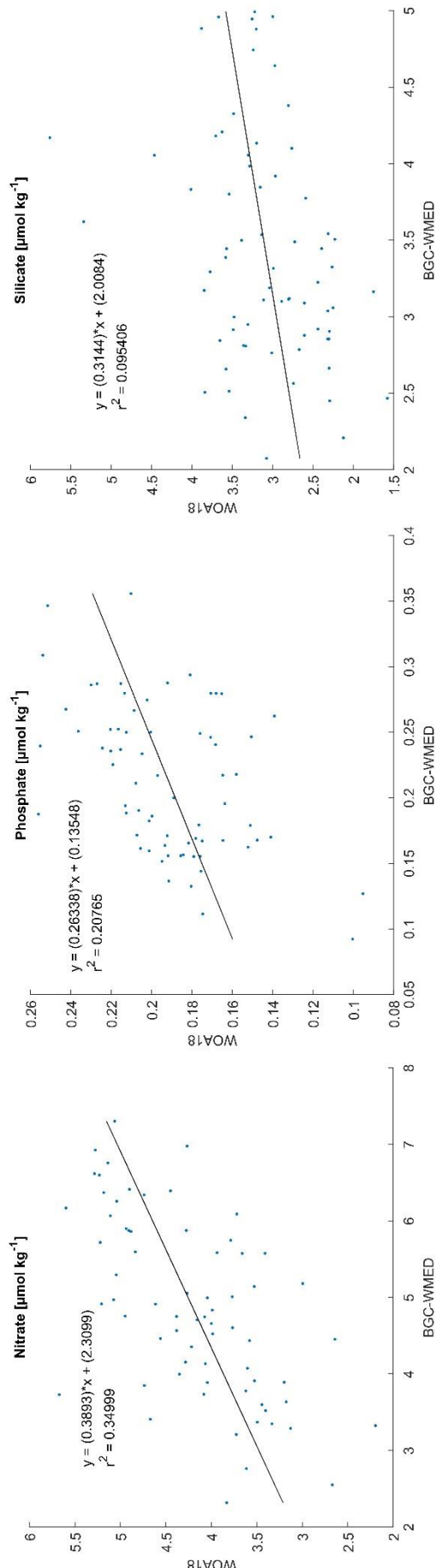


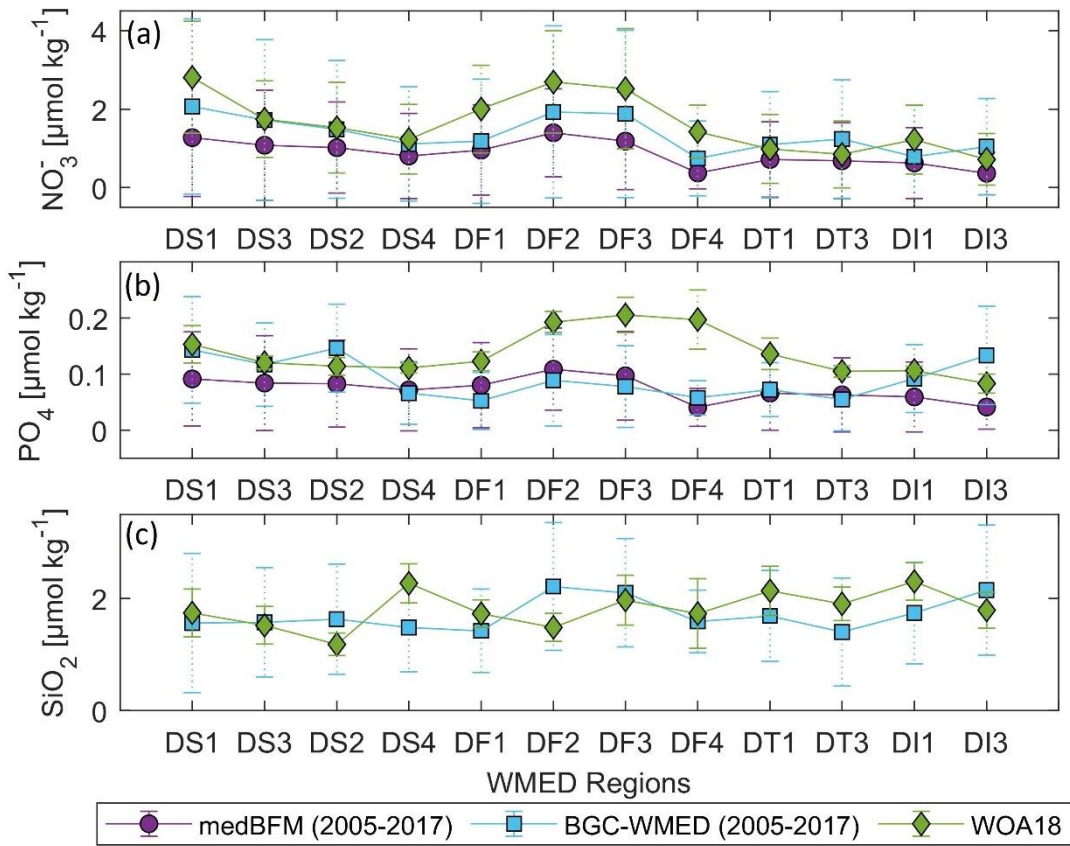
Figure 14. Scatterplot showing the WOA18 data as a function of the BCG-WMED climatology at 150 m with the regression line.

598 4.3.2 Regional horizontal comparison above 150 m average nutrient concentrations
599 The inorganic nutrient mean concentrations resulting from the climatology of this work (period 2005-
600 2017), and from both the medBFM reanalysis product and the WOA18 are compared in the upper layer
601 of 12 subregions of the WMED (in Table 4 and Fig. 15).
602 Results show a general agreement between BGC-WMED and the other two products in some
603 subregions, nonetheless, there are some differences as shown in section 4.3.1.
604 Upper layer nitrate average concentrations (Fig. 15a) are decreasing eastward, from the Alboran Sea
605 (DS1) to the Algerian basin (DS3, DS4) and the Balearic Sea (DS2). The western part of the basin is an
606 area under the direct influence of the inflowing Atlantic surface waters, where nitrate is known to be
607 present in excess compared to phosphate probably due to atmospheric N₂ input (Lucea et al., 2003). In
608 the DS1, BGC-WMED nitrate levels are lower than the WOA18 nitrate levels while in DS3, DS2 and
609 DS4 the average nitrate concentrations are similar to the WOA18.
610 From the Algerian basin (DS4, DF1) to Liguro-Provençal (DF3) regions, there is an increase in the
611 average nitrate in all products, this is the south-north gradient. Some difference arises, where the new
612 product is lower than the WOA18.
613 In the eastern regions, the lowest average concentrations of the WMED are found. Here, the difference
614 between products is smaller, with medBFM reanalysis being lower than the new product and the
615 WOA18.
616 As for phosphate (Fig. 15b), known to be the limiting nutrient of the WMED, because it is rapidly
617 consumed by phytoplankton (Lucea et al., 2003), its average levels are low in DS1, DS3, DS2 and DS4,
618 in WOA18, medBFM reanalysis and BGC-WMED. The latter did not agree well with the other products
619 in DS2, where it was slightly higher. Phosphate average concentrations slightly increase in DF1, DF2
620 and DF3 in all three products. The increase is explained by the vertical mixing process occurring in the
621 northern WMED.
622 Upper surface phosphate concentrations average start to decrease progressively through the Ligurian
623 East (DF4), Tyrrhenian Sea (DT1, DT3), Sardinia Channel (DI1) and Sicily Channel (DI3). The BGC-
624 WMED was in agreement with medBFM reanalysis in those subregions aside from concentrations in
625 DI3, where the new product showed higher levels.
626 The BGC-WMED climatology shows reasonable agreement in the upper average concentrations of
627 nitrate and phosphate that are similar in order of magnitude to the other products (Fig. 15). The
628 difference with the WOA18 resides in the wider temporal window of the observation (starting from

629 1955). The new climatology in some subregions has a better spatial coverage of in situ observation than
 630 the WOA18 (Garcia et al., 2019) and the medBFM reanalysis (Teruzzi et al., 2019).

631 On the other hand, the average silicate (Fig. 15c) of the new product and the WOA18 varied between
 632 regions. Significant difference is found between the two products in DS2, DS4, DF1, DF2, DT1, DT3,
 633 DI1 and DI3, while in DS1, DS3 and DF4 mean silicate is consistent between the two products.

634 Overall, the three products show strongly similar features between regions (similar curve shape).



635

636 **Figure 15.** Nutrient average concentrations and standard deviation comparison in the upper 150 m
 637 (values in Table 4).

638

639

640

641

642

643

644

645

646

647 **Table 4.** Nutrient average concentrations and standard deviation in the upper 150 m. All products were
 648 interpolated on 1° grid resolution (see Figure S2 (Belgacem et al., 2020)).

Subregion/ Coverage	Data product	Nitrate	Phosphate	Silicate
<i>DS1- Alboran Sea</i> (35°N– 37.3°N, -6°E– -1°E)	medBFM	1.27(±1.4)	0.09(±0.08)	-
	BGC-WMED	2.06(±2.2)	0.14(±0.09)	1.56(±1.2)
	WOA18	2.81(±1.4)	0.15(±0.03)	1.74(±0.4)
<i>DS3- Algerian West</i> (35.36°N– 38.3°N, -1°E– 4.3°E)	medBFM	1.07(±1.4)	0.08(±0.08)	-
	BGC-WMED	1.72(±2.05)	0.11(±0.07)	1.57(±0.9)
	WOA18	1.74(±0.9)	0.12(±0.01)	1.52(±0.3)
<i>DS2- Balearic Sea</i> (38.3°N– 42°N, -1°E– 4.3 °E)	medBFM	1.02(±1.1)	0.08(±0.07)	-
	BGC-WMED	1.48(±1.7)	0.14(±0.07)	1.63(±0.9)
	WOA18	1.53(±1.1)	0.11(±0.01)	1.18(±0.2)
<i>DS4- Algerian East</i> (36.3°N– 39.18°N, 4.3°E– 8.24°E)	medBFM	0.80(±1.08)	0.07(±0.07)	-
	BGC-WMED	1.11(±1.4)	0.06(±0.05)	1.48(±0.7)
	WOA18	1.23(±0.8)	0.11(±0.009)	2.27(±0.3)
<i>DF1- Algero-Provençal</i> (39.18°N– 41°N, 4.3°E– 9.18°E)	medBFM	0.96(±1.15)	0.08(±0.07)	-
	BGC-WMED	1.18(±1.5)	0.05(±0.05)	1.42(±0.7)
	WOA18	2.00(±1.1)	0.12(±0.01)	1.73(±0.2)
<i>DF2- Gulf of Lion</i> (42°N–43.36°N, 1°E–6.18°E)	medBFM	1.39(±1.19)	0.10(±0.07)	-
	BGC-WMED	1.92(±2.1)	0.08(±0.08)	2.21(±1.1)
	WOA18	2.68(±1.3)	0.19(±0.01)	1.48(±0.2)
<i>DF3- Liguro-Provençal</i> (41°N– 45°N, 6.18°E– 9.18°E)	medBFM	1.18(±1.2)	0.09(±0.07)	-
	BGC-WMED	1.88(±2.1)	0.07(±0.07)	2.10(±0.9)
	WOA18	2.52(±1.5)	0.20(±0.03)	1.97(±0.4)
<i>DF4- Ligurian East</i> (42.48°N–45°N, 9.18°E– 11°E)	medBFM	0.37(±0.4)	0.04(±0.03)	-
	BGC-WMED	0.74(±0.9)	0.05(±0.03)	1.59(±0.5)
	WOA18	1.42(±0.6)	0.19(±0.05)	1.73(±0.6)
<i>DT1- Tyrrhenian North</i> (39.18°N–42.48°N, 9.18°E– 16.16°E)	medBFM	0.71(±0.9)	0.06(±0.06)	-
	BGC-WMED	1.09(±1.3)	0.07(±0.04)	1.69(±0.8)
	WOA18	0.98(±0.8)	0.13(±0.02)	2.13(±0.4)
<i>DT3- Tyrrhenian South</i> (38°N– 39.18°N, 10°E– 16.16°E)	medBFM	0.68(±0.96)	0.06(±0.06)	-
	BGC-WMED	1.23(±1.5)	0.05(±0.05)	1.40(±0.9)
	WOA18	0.84(±0.8)	0.10(±0.01)	1.90(±0.2)
<i>DII- Sardinia Channel</i> (36°N– 39.18°N, 8.24°E– 10°E)	medBFM	0.62(±0.9)	0.05(±0.06)	-
	BGC-WMED	0.78(±1.3)	0.09(±0.06)	1.74(±0.9)
	WOA18	1.22(±0.8)	0.10(±0.007)	2.3(±0.30)
<i>DI3- Sicily Channel</i> (35°N– 38°N, 10°E–15°E)	medBFM	0.36(±0.5)	0.04(±0.03)	-
	BGC-WMED	1.04(±1.2)	0.13(±0.08)	2.15(±1.1)
	WOA18	0.72(±0.6)	0.08(±0.01)	1.79(±0.3)

649 4.3.3 Regional vertical comparison of nitrate and phosphate concentrations

650 As the last step in the comparison between the different products, it is investigated how the new
 651 climatology represents the vertical distribution by comparing the new climatological values for the
 652 period 2005-2017 with the medBFM reanalysis and the WOA18.

653 We extracted data values along a longitudinal transect across the Algerian basin in the west-east
654 direction (Fig. 16). The transect was selected according to previous studies (D'Ortenzio and Ribera
655 d'Alcalà, 2009; Lazzari et al., 2012; Reale et al., 2020) and since the Easternmost part of the domain is
656 showing markedly features, a transect across the Tyrrhenian Sea is extracted as well (Fig. 16). Silicate
657 is not included as it was not represented in the medBFM model.

658 Vertical sections of nitrate and phosphate in the Algerian Sea show a common agreement between
659 products about the main patterns found along the water column, i.e. the nutrient depleted surface layer
660 and the gradual increase toward intermediate depths, we note as well the west to east decreasing gradient
661 in the three products, yet, there are some inequalities.

662 Below 100 m, there is a significant difference between products and a poor qualitative agreement.
663 Nitrate distribution is dominated by the nutrient enriched IW, with high values ($>7 \mu\text{mol kg}^{-1}$) increasing
664 from east to west (Fig. 16). Phosphate shows similar patterns in the surface layer, exhibiting very low
665 concentration and a progressive increase down to 300 m ($> 0.35 \mu\text{mol kg}^{-1}$) noted also in the WOA18.
666 The reanalysis showed a more smoothed field, below 100-300 m, with phosphate concentration between
667 0.20 and $0.30 \mu\text{mol kg}^{-1}$. The highest values for phosphate were found below 250 m from 0°E to 3°E in
668 the new product. The BCG-WMED transect defines very well the different depth layers, the upper
669 intermediate layer is rich with nutrient concentration with $> 8 \mu\text{mol kg}^{-1}$ for nitrate (BGC-WMED) and
670 $>0.35 \mu\text{mol kg}^{-1}$ for phosphate (BGC-WMED and WOA18).

671 The vertical section along the Tyrrhenian Sea (Fig. 16) also shows a decrease from west to east in nitrate
672 concentrations. The same gradient is found also in phosphate in agreement with nutrient distribution
673 shown from the WOA18. From the section of the medBFM reanalysis, it is not easy to identify the west-
674 east gradient that we mentioned before. It could be suggested that the model under-estimate the vertical
675 features in the Eastern (Tyrrhenian Sea: 100-300 m, nitrate vary between 1.4 and $4.2 \mu\text{mol kg}^{-1}$,
676 phosphate between 0.13 and $0.20 \mu\text{mol kg}^{-1}$) and western part (Algerian basin: 100-300 m, nitrate vary
677 between 2.1 and $5.4 \mu\text{mol kg}^{-1}$, phosphate between 0.15 and $0.255 \mu\text{mol kg}^{-1}$). These values are lower
678 than the ones found in the BGC-WMED (Tyrrhenian Sea: 100-300 m, nitrate range between 3 to $6 \mu\text{mol}$
679 kg^{-1} , as for phosphate values oscillate between 0.10 - $0.27 \mu\text{mol kg}^{-1}$; Algerian basin: 100-300 m, nitrate
680 range between 3.6 to $8 \mu\text{mol kg}^{-1}$, as for phosphate values oscillate between 0.18 - $0.36 \mu\text{mol kg}^{-1}$).

681 While the WOA18 reproduces similar patterns as the new climatology (Tyrrhenian Sea: 100-300 m,
682 nitrate vary between 1.8 and $5.7 \mu\text{mol kg}^{-1}$, phosphate between 0.33 and $0.20 \mu\text{mol kg}^{-1}$) and western
683 part (Algerian basin: 100-300 m, nitrate vary between 2.8 and $6.8 \mu\text{mol kg}^{-1}$, phosphate between 0.16
684 and $0.34 \mu\text{mol kg}^{-1}$).

685 The products illustrate the nutrient-poor water in the eastern side (Tyrrhenian Sea) and the relatively
686 nutrient-rich water found in the western transect (Algerian basin).

687 The BGC-WMED product captures details in Fig. 16 about the longitudinal gradient in nitrate and
688 phosphate, along the water column where nutrient sink deeper from west to east as previously seen in
689 Pujo-Pay et al. (2011) and Krom et al. (2014), an increased oligotrophy from west to east with higher
690 concentrations in the two nutrients in the western side of the section and a more oligotrophic character
691 toward east.

692 The differences between products could be explained by the difference in the data coverage, time span
693 and the difference in methods used to construct the climatological fields.

694 The variability in nitrate and phosphate fields along the transect extracted from the BGC-WMED reflects
695 the high resolution of the product allowing the screening of vertical structure controlling nutrient
696 contents. Based on a visual comparison, the new product is able to reproduce similar patterns as to the
697 WOA18 and to a lesser extent the medBFM reanalysis.

698 Fig. 17 examines the vertical difference of nitrate and phosphate concentration for the BGC-WMED
699 with the medBFM reanalysis along the Algerian basin (Fig.17a, nitrate; Fig.17b, phosphate) and
700 WOA18 (Fig.17c, nitrate; Fig.17d, phosphate).

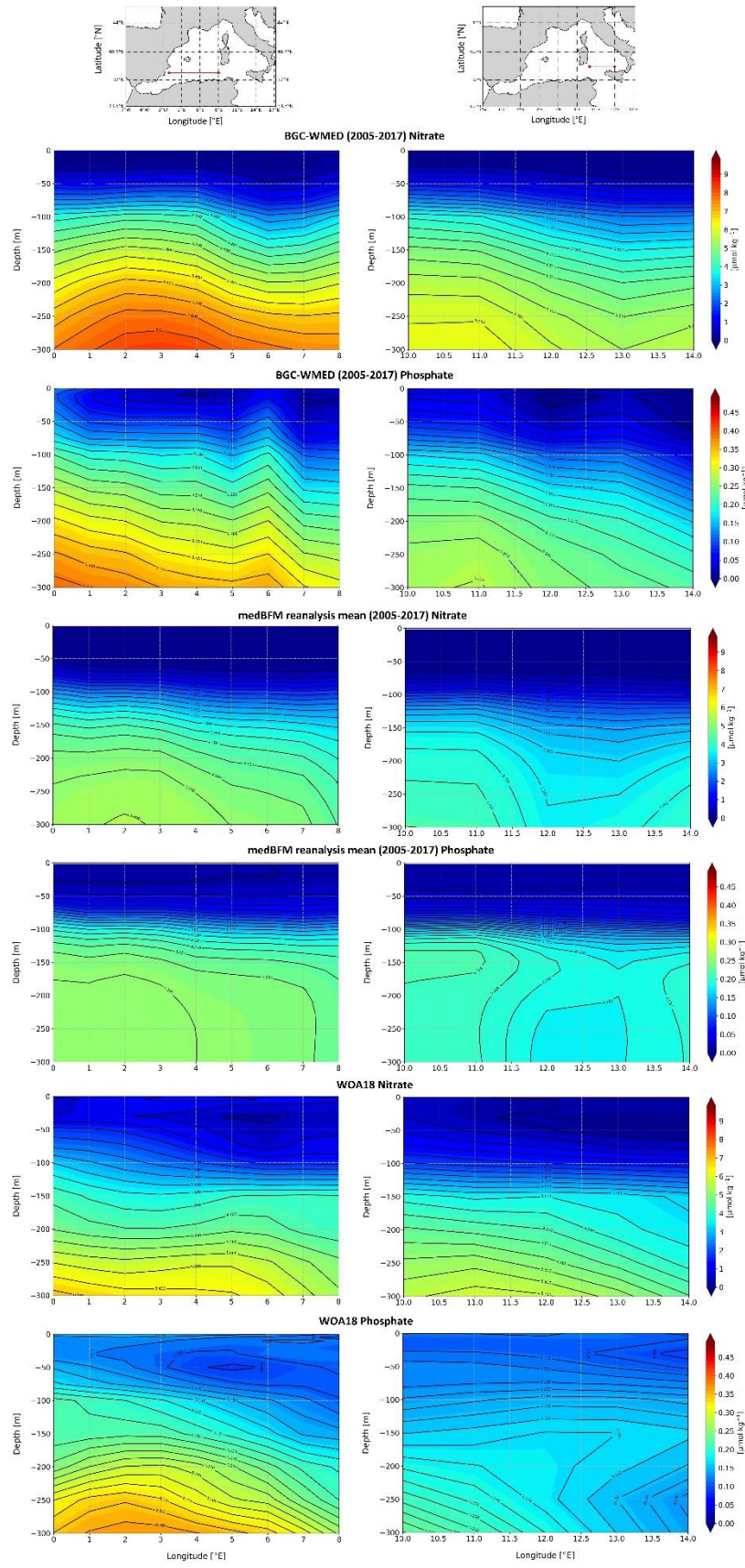
701 The vertical section shows a strong agreement at the surface for nitrate between the BGC-WMED and
702 the medBFM reanalysis (Fig. 17a), while the vertical difference with WOA18 demonstrates that nitrate
703 values in the new product are lower than the WOA18 at 50- 75 m (Fig. 17c).

704 The difference increases with depth, below 100 m, the BGC-WMED nitrate climatology is higher than
705 the medBFM with a difference ranging between 0.6 and 2.4 $\mu\text{mol kg}^{-1}$, similar observation is noted in
706 the WOA18 (Fig. 17c). In Fig.17a and Fig.17c, we identify patterns in the vertical structure of nitrate
707 in the eastern portion of the transect.

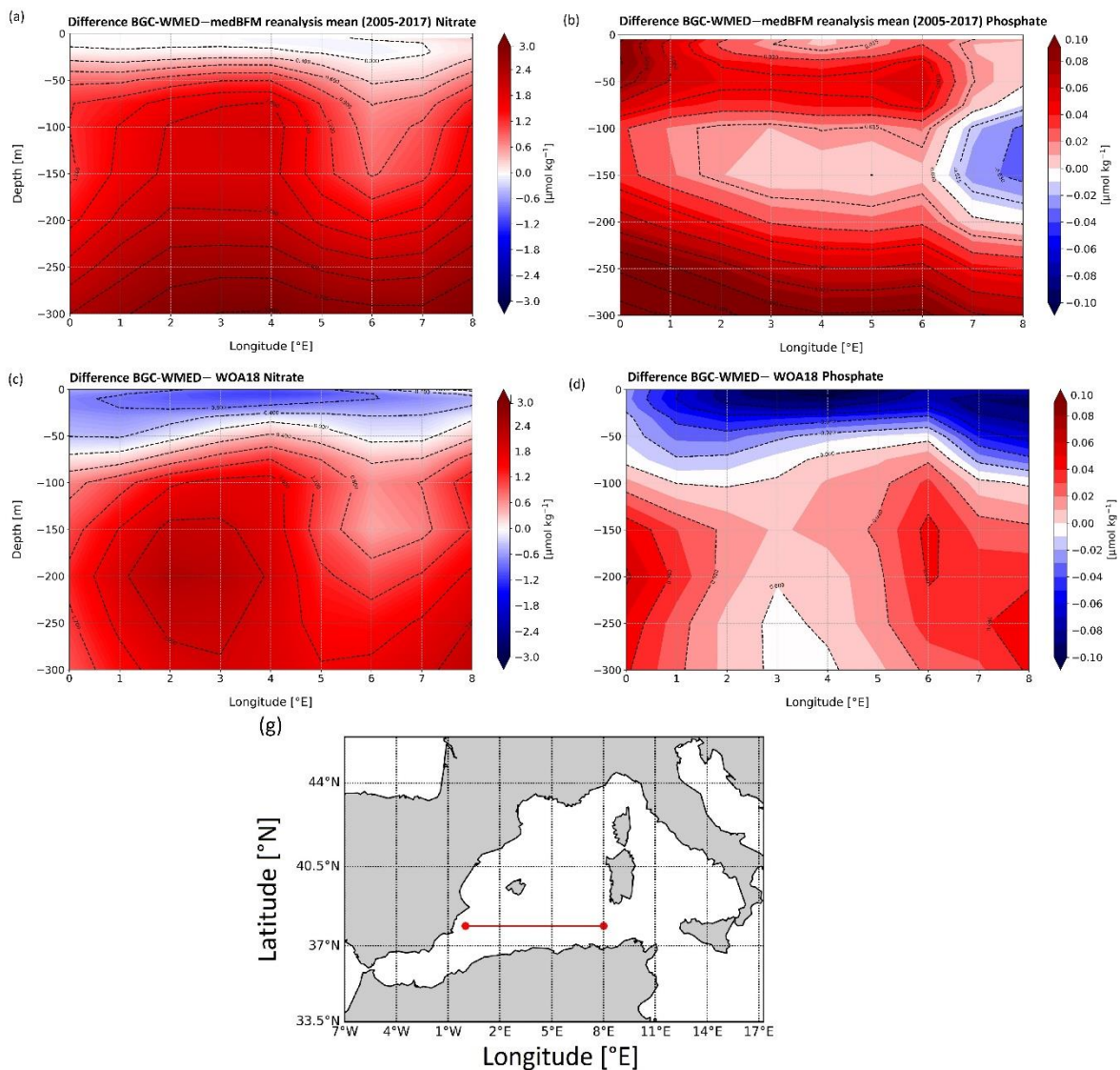
708 Regarding phosphate, differences between the new climatology and the medBFM reanalysis are noted
709 (Fig. 17b) where the BGC-WMED shows high concentrations in the first 100 m and between 150 m and
710 300 m (differences of 0.02 - 0.08 $\mu\text{mol kg}^{-1}$), this difference decreases at 100-150 m. At the eastern
711 portion of the transect (6°E to 7.5°E), we find an agreement between the two products.

712 Conversely, the vertical sections of the differences between BGC-WMED and WOA18 in phosphate
713 (Fig.17 d) show similarities, with the new product being lower than the WOA18 in the first 50 m. Large
714 difference is found on both sides of the transect below 100 m, while in the center of the transect, the
715 difference in phosphate is reduced to 0-0.02 $\mu\text{mol kg}^{-1}$.

716 Fig.18 compares the vertical difference of nitrate and phosphate along the Tyrrhenian Sea transect. In
717 general, the difference transect in the Tyrrhenian Sea shows similar features with medBFM reanalysis
718 and the WOA18 as in Algerian basin. Fig.18d captures the west to east gradient in phosphate. The
719 WOA18 overestimated phosphate in the surface layer.

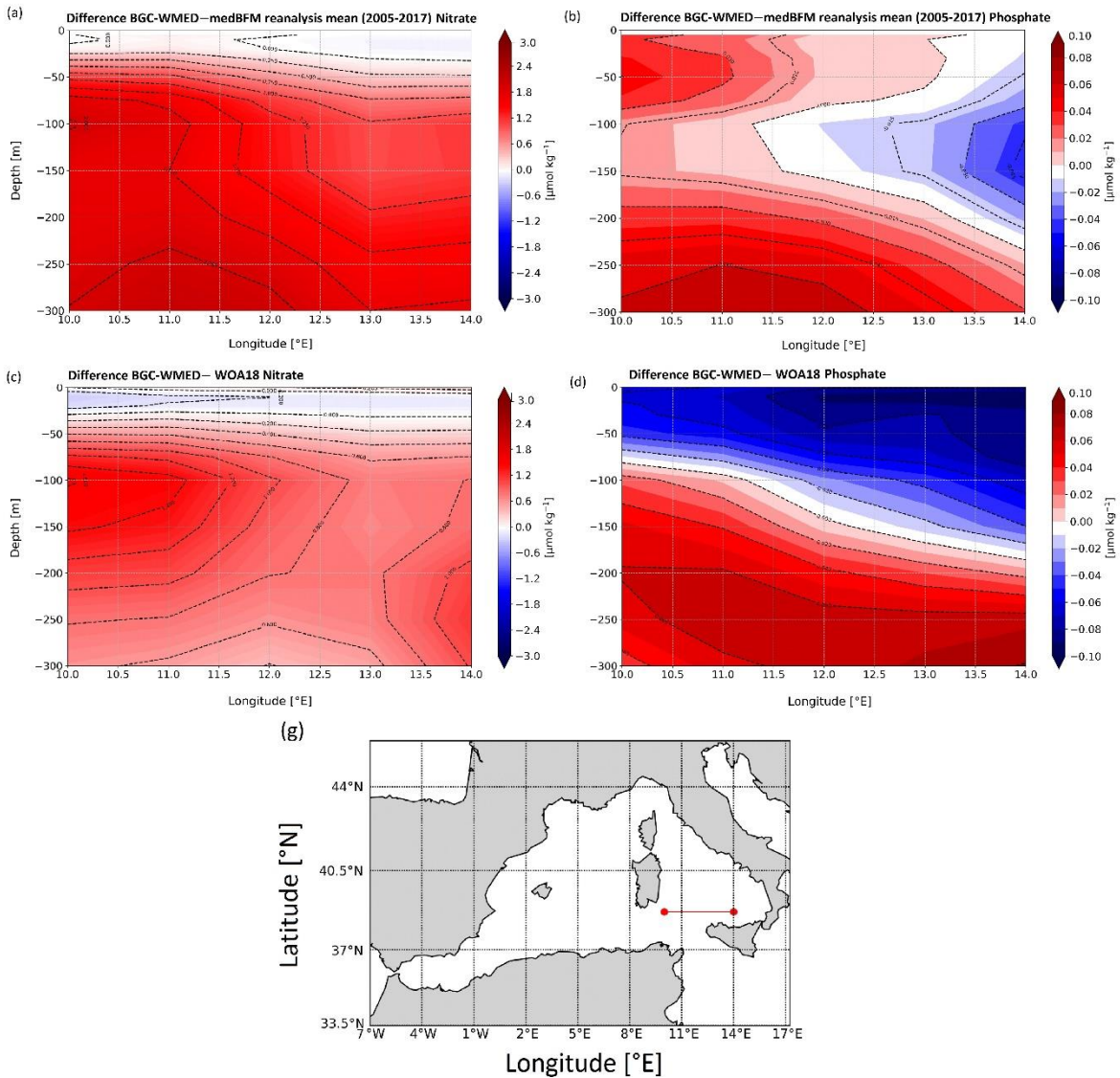


721 **Figure 16.** Vertical distribution of nitrate and phosphate from the Algerian basin and Tyrrhenian Sea.
722 Colors show the gridded values from the three different products: BGC-WMED, medBFM reanalysis
723 (Teruzzi et al., 2019) and the WOA18 (Garcia et al., 2019).
724 Based on the new climatology comparison with the WOA18 and the reanalysis, it is concluded that the
725 new product is consistent with the main features of previous products and show the large-scale patterns
726 and underline well the characteristics of the water mass layers.
727 The study also provides an examination of the nitrate and phosphate distributions along a longitudinal
728 transect across the Algerian Basin (Western WMED) and across the Tyrrhenian Sea (Eastern WMED).
729 We have shown that the western basin is relatively high in nutrients compared to the Eastern basin. The
730 increased oligotrophic gradient from west to east could be attributed to the difference in the
731 hydrodynamic patterns related to the water mass specific properties that are affected by the EMED and
732 the Atlantic ocean inflows, and to the local sources of nutrients (Ribera d'Alcalà et al., 2003; Schroeder
733 et al., 2010). Study of Crispi et al. (2001) inferred the biological activity that is responsible for the
734 oligotrophic gradient.



735

736 **Figure 17.** Difference of vertical section from the Algerian basin between BGC-WMED and medBFM
 737 (a. nitrate, b. phosphate), BGC-WMED and WOA18 (c. nitrate, d. phosphate), with dashed contour lines
 738 and labels.



739

740 **Figure 18.** Same as Fig.17 but for the vertical section from the Tyrrhenian Sea.

741 4.4 Temporal comparison: 1981-2004 vs 2005-2017

742 In this section, we compare between two climatological periods (1981-2004 vs 2005-2017). The
 743 distinction between the two periods was based on the occurrence of the Western Mediterranean
 744 Transition (WMT) that started in 2004/05, during which there was a progressive increase in temperature
 745 and salinity of the IW that led to important deep convection events, substantially increasing the rate of
 746 DW formation between 2004 and 2005 (Schroeder et al., 2016).

747 The result of this climatological event was that a newly generated DW, denser, saltier, and warmer than
 748 the old WMDW, filled up the WMED. The new WMDW propagated east toward the Tyrrhenian Sea
 749 and west toward the Alboran Sea and Gibraltar (Schroeder et al., 2016).

750 A recent study of Li and Tanhua (2020) demonstrated an enhanced ventilation in the WMED deep layers
 751 despite the continuous overall increase in temperature (Bindoff et al., 2007), salinity and density of

752 intermediate and deep layers after the WMT (Schroeder et al., 2016; Vargas-Yáñez, 2017). An increased
753 ventilation means a DW renewal (Schroeder et al., 2016; Tanhua et al., 2013) subsequently a well
754 oxygenated waters, implying an increase in the decomposition of the sinking organic matters into
755 inorganic nutrients, thus causing changes of biogeochemical cycles (Shepherd et al., 2017). What
756 happened in the WMED was not a permanent continuous event, since DW formation faded during the
757 years 2006 and 2007, to restart again in 2008 (Li and Tanhua, 2020). In this section, we investigate the
758 possible impact of WMT on biogeochemical characteristics at different depth levels (with a focus on
759 nitrate, phosphate and silicate regional distribution and patterns).

760 We considered depth levels that represent the usual three layers: the surface (100 m; Fig.19a,d-20a,d-
761 21a,d), intermediate (300 m; Fig.19b,e- 20b,e- 21b,e) and deep layers (1500 m; Fig.19c,f -20c,f- 21c,f).

762 The WMED surface layer is dominated by the AW coming through the Alboran Sea, a permanent area
763 of upwelling (García-Martínez et al., 2019), where there is a continuous input of elements from the layer
764 below to the surface (Fig. 19a- 20a- 21a). Nitrate increased after WMT (Fig. 19d- 20d- 21d) by +0.4137
765 $\mu\text{mol kg}^{-1}$ (Fig. A4a). The largest difference between the two periods reached $>+2 \mu\text{mol kg}^{-1}$ in Sardinia
766 Channel and the Alboran Sea that was explained by the favorable conditions for nitrogen fixation as
767 discussed in Rahav et al. (2013), revealing also that nitrogen fixation rate increased from east-to-west.
768 Phosphate and silicate on the other hand described a decrease at 100 m (Fig. A4a) with about -0.021 and
769 $-0.1365 \mu\text{mol kg}^{-1}$ on average, respectively. Large changes are noticed in the southern Alboran Sea,
770 Sardinia channel and Balearic Sea.

771 The surface layer exhibits an irregular distribution since it is subjected to seasonal variability. We found
772 an increase in all nutrients at 300 and 1500 m with a maximum identified at intermediate depths in both
773 nitrate and phosphate which is explained by the remineralization of organic matter along the path of the
774 IW. The latter flows westward (from the Levantine to the Atlantic Ocean). Its content in nutrients
775 increases (relatively to the conditions in the EMED) with age (Schroeder et al., 2020). It arrives at the
776 Tyrrhenian Sea, where in Fig.19b-20b-21b (at 300 m depth, 1981-2004), we identify a nutrient-depleted
777 intermediate layer. At this depth level, we observe a gain in the three nutrients after WMT (Fig.19e-20e-
778 21e). On average, the difference between the two periods (pre/post-WMT) for nitrate, phosphate, and
779 silicate, is around $+0.8648$, $+0.0068$ and $+0.2072 \mu\text{mol kg}^{-1}$ (Fig. A4b), respectively.

780 A similar increase after WMT in the deep layer (1500 m), is also found for nutrient concentrations (Fig.
781 19f, 20f, 21f) in the magnitude of $+0.753$ for nitrate, $+0.025$ for phosphate, and $+0.867$ for silicate (Fig.
782 A4c), which highlights an increase in the downward flow of organic matter remineralization that is
783 supplying the existing pool.

784 This increase is also illustrated in the climatological mean vertical profile of Fig. 22 in the three
785 nutrients. Nitrate displays a notable vertical difference to the pre-WMT period below 200 m (Fig. 22a).
786 Phosphate difference between the two-time period is larger below 400 m (Fig. 22b). Silicate was
787 different from nitrate and phosphate. It increases progressively with depth (Fig.22c) and demonstrates

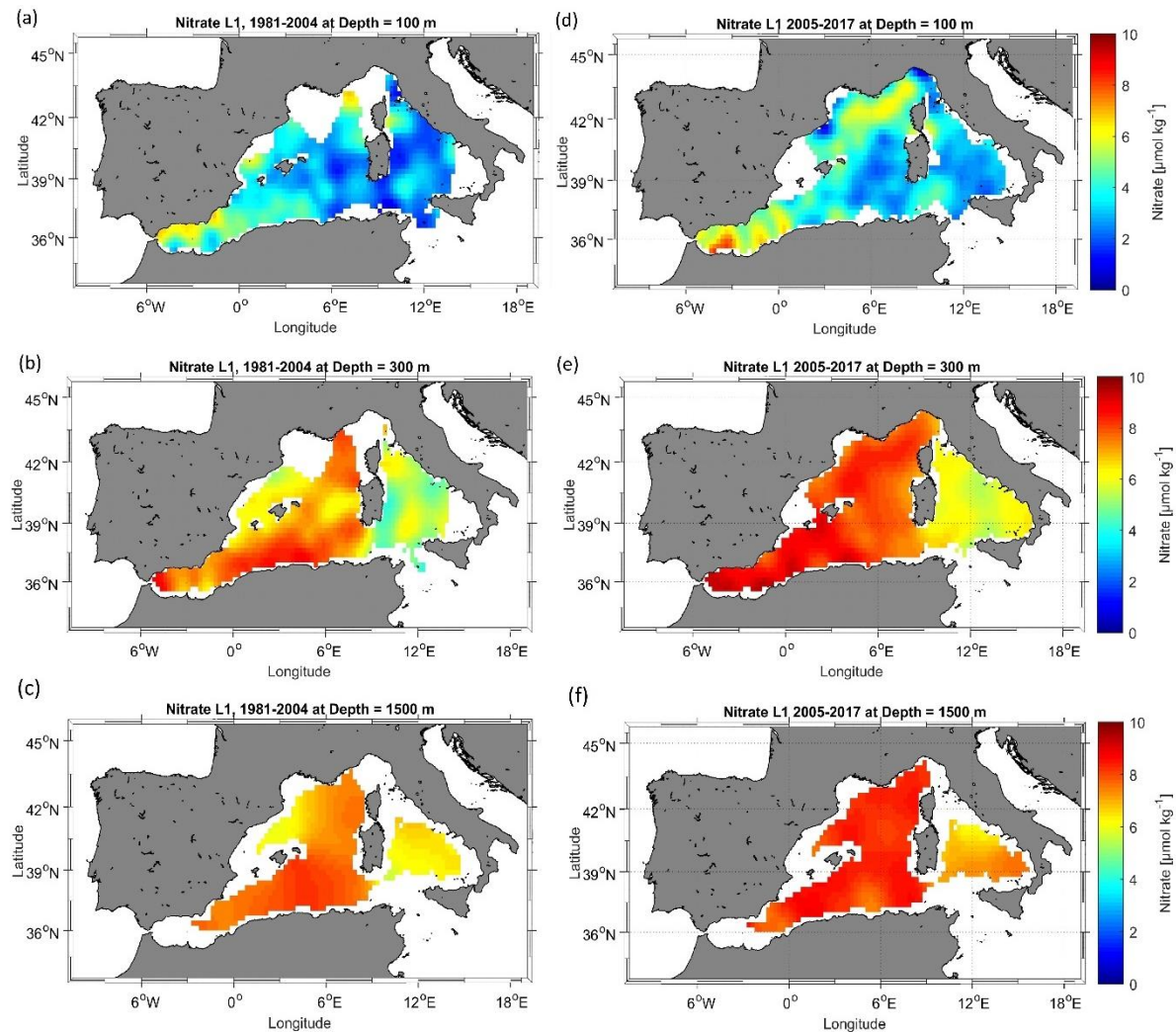
788 an enrichment of the DW compared to the 1981-2004 period (Fig. 21c). The maximum values are found
789 in the deep layer, due to the low remineralization rate. With the warming climate, biogenic silica tends
790 to dissolve faster which explains the high concentrations all over the basin even the Tyrrhenian Sea after
791 the WMT.

792 According to Stöven and Tanhua (2014), the impressive volume of the newly formed DW during 2004
793 and 2006, ventilated the old DW decreasing its age, meaning that the WMT could have led to the
794 lowering of the WMED deep layer pool in nutrient as it was pointed out by Schroeder et al. (2010).
795 However, we did not observe this decrease in the climatological analysis after the WMT. It might be
796 due to the temporal variability of the deep convection intensity, since a decrease has been recorded in
797 the Gulf of Lion between 2007 and 2013 (Houpert et al., 2016).

798 A decrease in the deep convection intensity since the WMT (Houpert et al., 2016; Li and Tanhua, 2020),
799 could potentially lead to the reduction in the supply from the nutrient-rich DW (before WMT) to the
800 surface, i.e. the decrease in nutrient could have happened right after the WMT in spring 2005 where
801 Schroeder et al. (2010) reported peculiar divergence between the old WMDW and the new WMDW in
802 nitrate and phosphate; the new WMDW was low in nutrient; later on an intense DW formation event
803 marked the year 2012 with a strong ventilation that has been recorded in the Adriatic Sea that could
804 have affected the WMED. It was not possible to observe this change since we calculated the mean state
805 of the basin spanning a specific period.

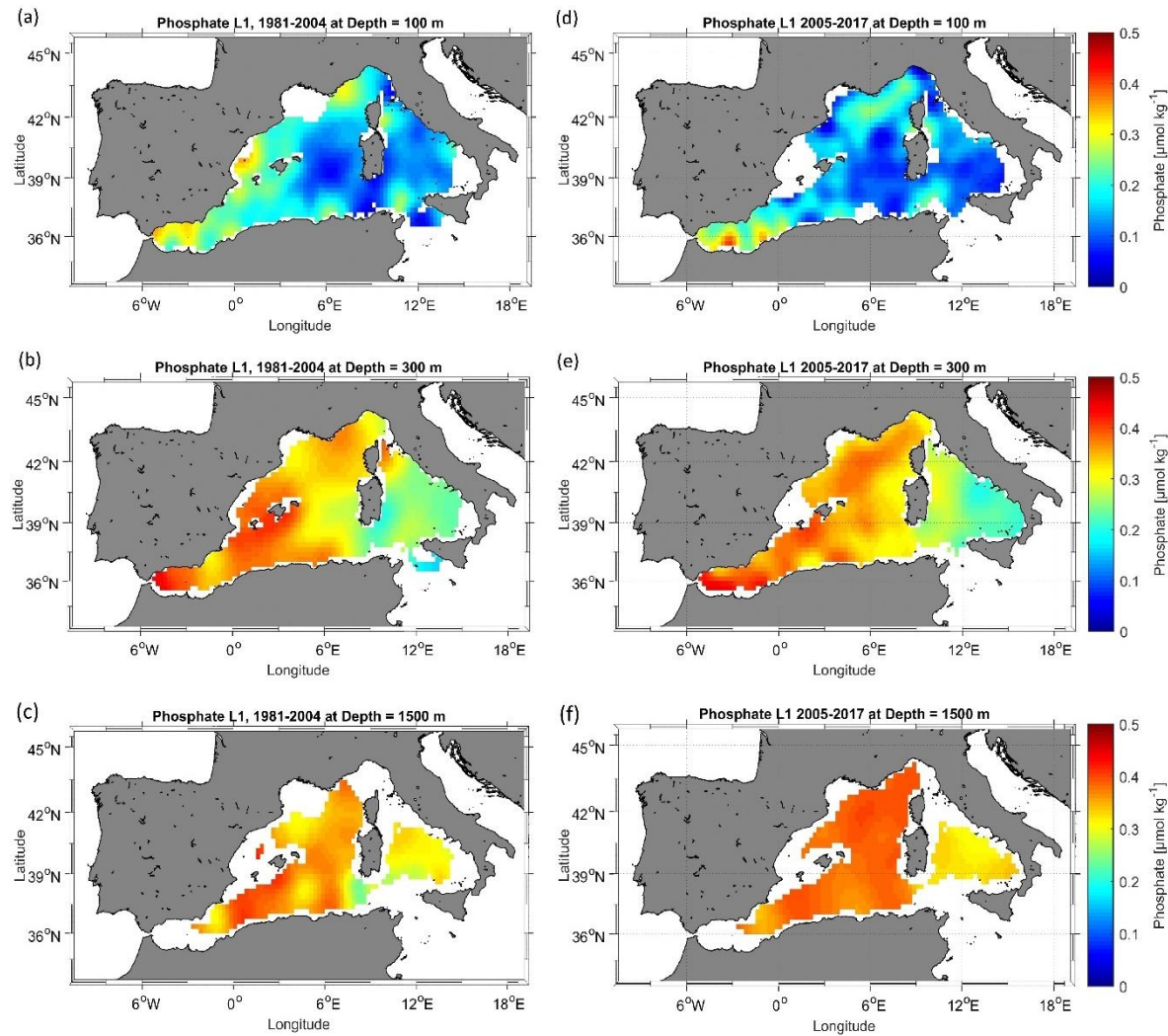
806 The spatial distribution of nutrient concentrations after the WMT (2005-2017) was quite different from
807 the one before the WMT (1981-2004). This could also be related to the significant decline in river
808 discharge between 1960 and 2000, which was estimated to 20% (Ludwig et al., 2009). The decrease is
809 also observed in silicate fluxes since silicate loads through river discharge.

810 The change could be explained by the low denitrification rate for nitrate and an increase in the
811 remineralization of organic matter. Ludwig et al. (2009) reported an increase in nitrate and phosphate
812 fluxes that was enhanced by the anthropogenic inputs, loading the deep layer with inorganic nutrients,
813 also it could be associated with the slower ventilation of the WMED waters and a longer residence time.



814

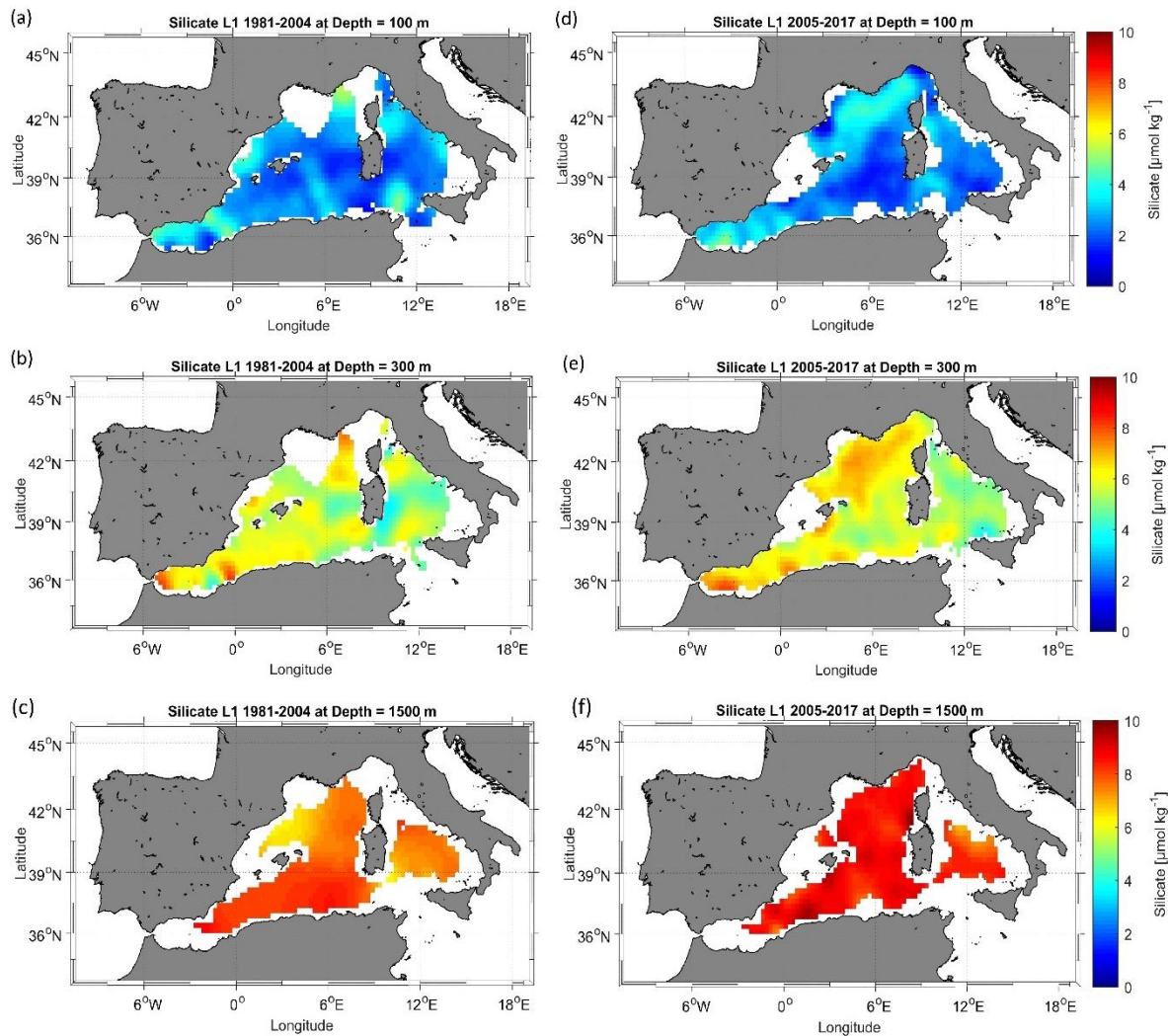
815 **Figure 19.** Nitrate climatological field (masked analysis fields masked using relative error threshold =
816 0.3 (L1)) at 100 m, 300 m, and 1500 m, for two periods: 1981-2004 (a, b, c) and 2005-2017 (d, e, f).



817

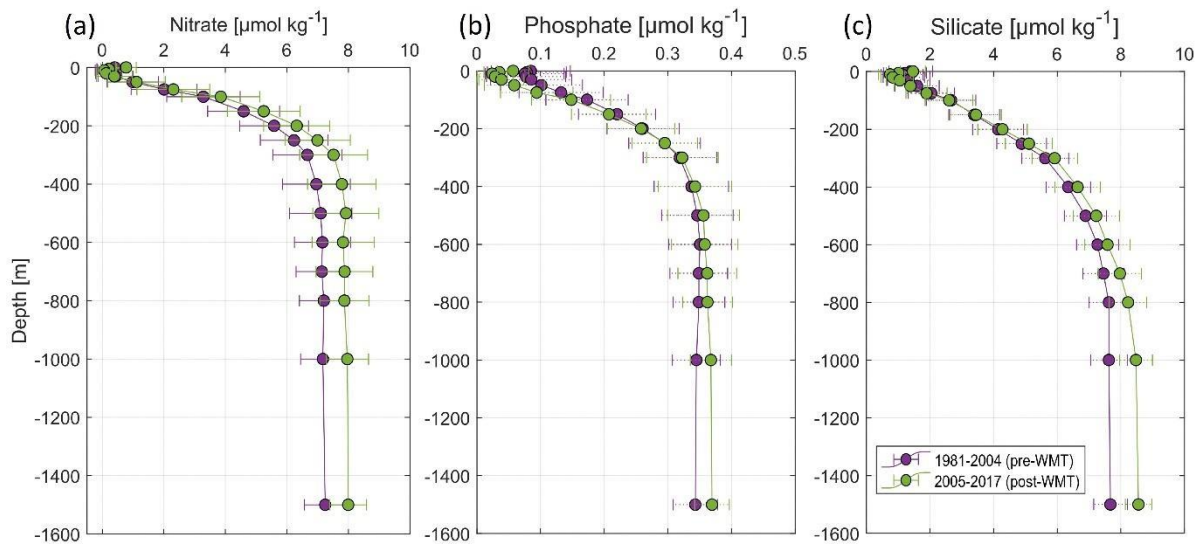
818 **Figure 20.** The same as Fig. 19 but for phosphate.

819



820

821 **Figure 21.** The same as Fig. 19 but for silicate.



822

823 **Figure 22.** Climatological mean vertical profile and standard deviation of (a) nitrate, (b) phosphate and
824 (c) silicate over the WMED before (1981-2004, in violet) and after WMT (2005-2017, in green).

825 **5 Data availability**

826 The climatologies of Nitrate, Phosphate and Silicate are available as netCDF files from the data
827 repository PANGAEA and can be accessed at <https://doi.org/10.1594/PANGAEA.930447> (Belgacem
828 et al., 2021). Ancillary information is in the readme in PANGAEA with the list of variables that are
829 described in table 3 of section 4. The CNR_DIN_WMED_20042017 data are available from PANGAEA
830 (<https://doi.org/10.1594/PANGAEA.904172>). The MOOSE-GE data are available in the SISMER
831 database (global doi[10.18142/235](https://doi.org/10.18142/235))

832 **6 Conclusion**

833 In this study, we investigated spatial variability of the inorganic nutrients in the WMED and presented
834 a climatological field reconstruction of nitrate, phosphate, and silicate, using an important collection
835 dataset spanning 1981 and 2017. The BGC-WMED new product is generated on 19 vertical levels on a
836 1/4° spatial resolution grid.

837 The new product represents very well the spatial patterns about nutrient distribution because of its higher
838 spatial and temporal data coverage compared to the existing climatological products (see Table 1), it is
839 contributing to the understanding of the spatial variability of nutrients in the WMED.

840 The novelty of the present work is the use of the variational analysis that takes into consideration
841 physical, geographical boundaries, topography, and the resulting estimate of the associated error field.

842 Comparison with previously reported studies gives that the BGC-WMED reproduces common features
843 and agrees with previous records. The reference products WOA18 and medBFM biogeochemical
844 reanalysis tend to underestimate nutrient distribution in the region with respect to the new product.

845 The new product captures the strong east-west nutrient gradient and vertical features. The results
846 obtained do not include seasonal or annual analysis fields. However, the aggregated dataset here does
847 show improvements in describing the spatial distribution of inorganic nutrients in the WMED. We
848 acknowledge that computing a climatological mean over a time period is not enough to estimate and
849 detect the climate shift ‘WMT’ change driven trend. However, comparing climatologies based on the
850 two time periods: 1981-2004 (pre-WMT) and 2005 -2017 (post-WMT) has already produced important
851 results. Notable changes have been found in nutrient distribution after the WMT at various depths.

852 The results support the tendency to a relative increasing load of inorganic nutrients to the WMED and
853 possibly relate the change in general circulation patterns, changes in deep stratification and warming
854 trends, however, this remains to be evidenced.

855 The BGC-WMED is a regional climatology that has allowed the identification of a substantial
856 enrichment of the waters, except for the Tyrrhenian Sea where the water column is depleted in nutrients

857 with respect to the western areas of the WMED. The climatology gave information about the spreading
 858 of inorganic nutrients inside the WMED at surface, intermediate and deep layers.
 859 A future work will suggest a better understanding of the change in nutrients related to water masses
 860 associated with ventilation rate, a climatological field along isopycnal surfaces instead of depths and the
 861 correlation between potential temperature and nutrients.

862 **Appendix A: Additional information about cruise metadata**

863 **Table A1.** Summary table of the analytical techniques and instruments used for nutrient analysis.

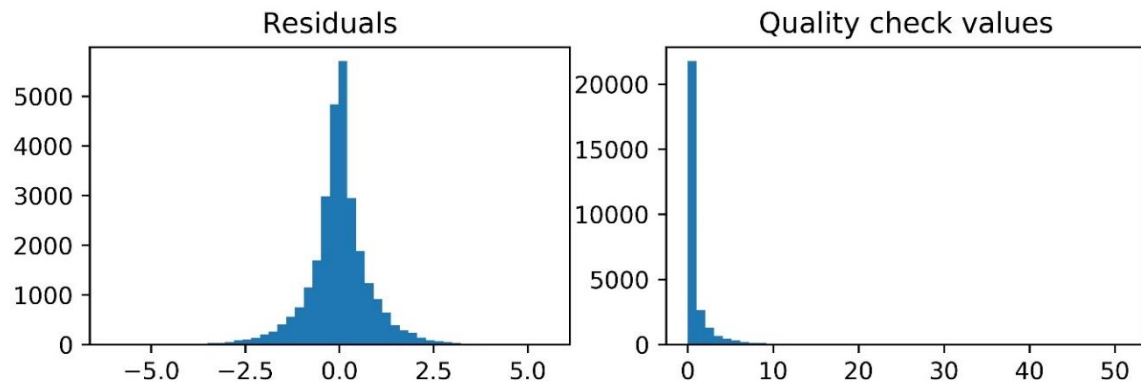
Data source	Analytical methods	Reference
MEDATLAS	-flow analysis system (autoanalyser) equipped with Chemlab -technicon colorimeters.	http://www.ifremer.fr/mater/dataset_i/chemitt.html
SEADATANET including MOOSE-GE	-flow analysis system (autoanalyser) equipped with Bran-Luebbe Seal	https://www.obs-banyuls.fr/fr/observer/moose.html https://mistral.sedoo.fr/?editDatsId=1351&dataId=1351&project_name=MOOSE
CNR_DIN_WMED_20042017	-continuous-flow system multichannel (Auto Analyzer Bran+Luebbe III Generation -OI-Analytical (Flow Solution III) flow-segmented -Systea discrete analyzer EasyChem Plus	Belgacem et al., (2020) https://doi.org/10.5194/essd-12-1985-2020
Other cruises: Medship programs; GLODAPv2; CARIMED	nutrient analysis strictly followed the recommendation of the World Ocean Circulation Experiment (WOCE) and the GO-SHIP protocols example: Quattro auto-analyzer from SEAL analytics.	Schroeder et al., (2015) Tanhua et al., (2013) https://doi.org/10.5194/essd-5-289-2013 Olsen et al., (2016) Hydes et al., (2010)

864

865 **Appendix B: Additional information about quality assurance**

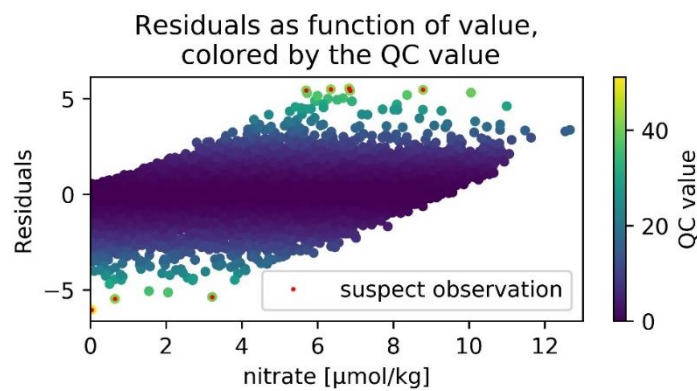
866 **Table A2.** Summary of the quality check analysis quality assurance of 1981-2017 climatology.

RMS	Nitrate	Phosphate	Silicate
Pre-quality check	0.848	0.05	0.763
Post-quality check	0.838	0.049	0.757
Number of suspected points	10	6	2



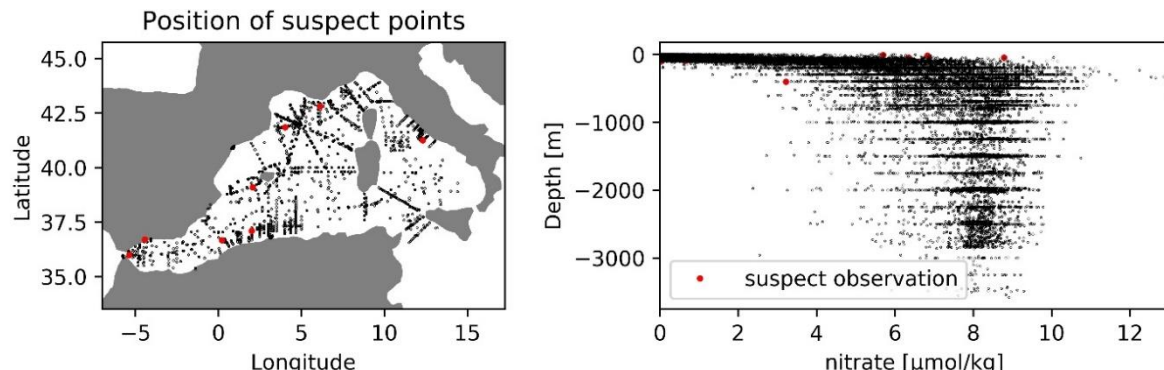
867

868 **Figure A1.** Overview of residual distribution and quality check values for Nitrate gridded fields
 869 (1981-2017) before the quality check.



870

871 **Figure A2.** Scatterplot of residual as function of nitrate values (1981-2017) colored by the quality
 872 check values. The red dots are the suspect observation (points with qcvalues > 40).



873

874 **Figure A3.** Position of the suspect points (nitrate climatology, 1981-2017).

Appendix C: Additional information about temporal comparison

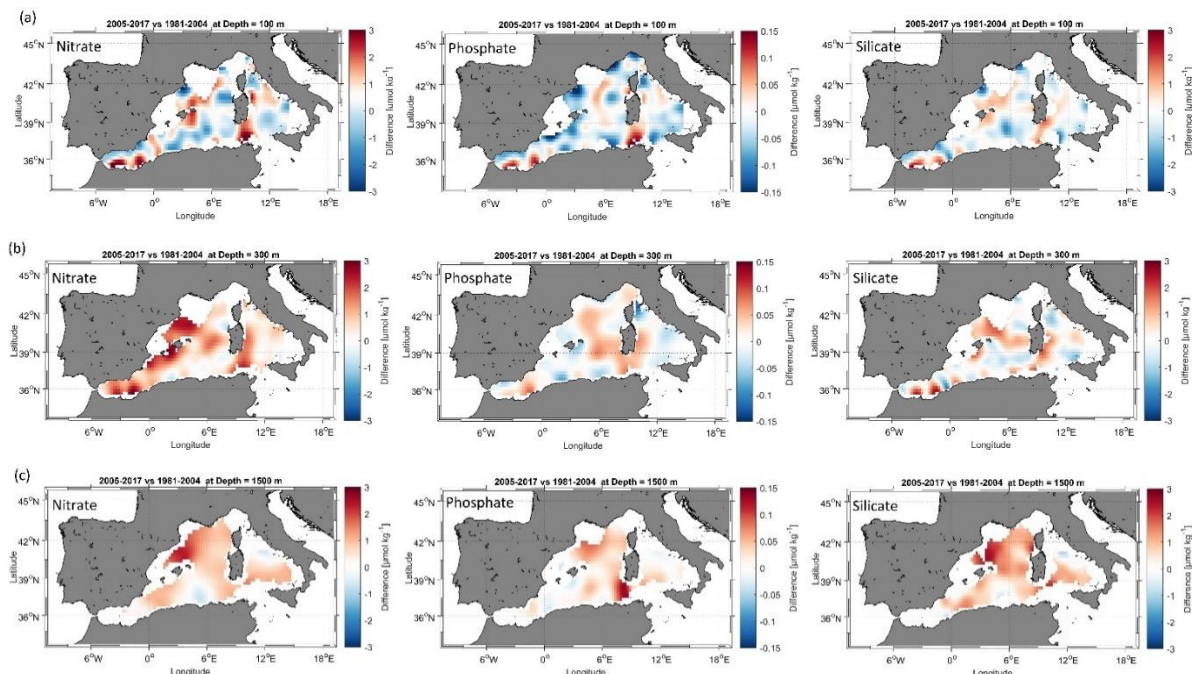


Figure A4. (a) Difference field at 100 m between the 1981-2004 climatology and the 2005-2017 climatologies; (b) Difference field at 300 m (c) Difference field at 1500 m.

Author contributions

The BGC-WMED climatology product was led between the CNR-ISMAR and DAIS- University of Venice. MBe, KS and JC designed the experiment and contributed to the writing of the manuscript. AB and CT helped MB to perform the analysis and contributed to the manuscript. BP contributed to specific parts of the manuscript. MBo contributed to data collection. PR and NG contributed to nutrient analyses during the MOOSE cruises in the northern Mediterranean Sea.

Acknowledgements

Data was provided through SeaDataNet Pan-European infrastructure for ocean and marine data management (<https://www.seadatanet.org>), Mediterranean Ocean Observing System for the Environment, MOOSE (<http://www.moose-network.fr/>), thanks to the work of MBo, PR and NG (MIO, Mediterranean Institute of Oceanography) during the last 10 years. MBe acknowledge the WOA18 and CMEMS for the medBFM data (<https://www.cmcc.it/doi/mediterranean-sea-biogeochemical-analysis-and-forecast-cmems-med-biogeochemistry>). We wish to thank all colleagues who contributed to the data acquisition, and the PIs of the cruises involved. MBe thanks Kanwal Shahzadi from the University of Bologna for the discussions during our internship at GHER, University of Liège. We are grateful to the Institut National des Sciences de l'Univers (CNRS-INSU) and European projects for supporting the MOOSE network. JC and KS acknowledge several of national and European projects, e.g.: KM3NeT, EU GA #011937; SESAME, EU GA #GOCE-036949; PERSEUS, EU GA #287600; OCEAN-

899 CERTAIN, EU GA #603773; COMMON SENSE, EU GA #228344; EUROFLEETS, EU GA #228344;
900 EUROFLEETS2, EU GA # 312762; JERICO, EU GA #262584; the Italian PRIN 2007 program
901 “Tyrrhenian Seamounts ecosystems”, and the Italian RITMARE Flagship Project, both funded by the
902 Italian Ministry of University and Research.

904 **References**

905 Barnes, S.L. (1964). A technique for maximizing details in numerical weather map analysis. *J. App. Meteor.*, 3, 396-409.

906 Barnes, S.L. (1994). Applications of the Barnes Objective Analysis Scheme, Part III: Tuning for Minimum Error. *J. Atmosph. and Oceanic Tech.*, 11, 1459-1479.

907 Barth, A., Troupin, C., Alvera-Azcárate, A. and Vandenbulcke, L.: Divand-1.0: N-dimensional variational data analysis for ocean observations, *Geosci. Model Dev.*, 7(1), 225–241, doi:10.5194/gmd-7-225-2014, 2014.

908 Beckers, J. M., Barth, A., Troupin, C. and Alvera-Azcárate, A.: Approximate and efficient methods to assess error fields in spatial gridding with data interpolating variational analysis (DIVA), *J. Atmos. Ocean. Technol.*, 31(2), 515–530, doi:10.1175/JTECH-D-13-00130.1, 2014.

909 Belgacem, M., Chiggiato, J., Borghini, M., Pavoni, B., Cerrati, G., Acri, F., Cozzi, S., Ribotti, A., Álvarez, M., Lauvset, S. K. and Schroeder, K.: Dissolved inorganic nutrients in the western Mediterranean Sea (2004-2017), *Earth Syst. Sci. Data*, 12(3), 1985–2011, doi:10.5194/essd-12-1985-2020, 2020.

910 Bethoux, J. P., Morin, P., Madec, C. and Gentili, B.: Phosphorus and nitrogen behaviour in the Mediterranean Sea, *Deep Sea Res. Part A, Oceanogr. Res. Pap.*, 39(9), 1641–1654, doi:10.1016/0198-0149(92)90053-V, 1992.

911 Brankart, J. M. and Brasseur, P.: The general circulation in the Mediterranean Sea: A climatological approach, *J. Mar. Syst.*, 18(1–3), 41–70, doi:10.1016/S0924-7963(98)00005-0, 1998.

912 Brasseur, P., Beckers, J. M., Brankart, J. M. and Schoenauen, R.: Seasonal temperature and salinity fields in the Mediterranean Sea: Climatological analyses of a historical data set, *Deep. Res. Part I Oceanogr. Res. Pap.*, 43(2), 159–192, doi:10.1016/0967-0637(96)00012-X, 1996.

913 Brasseur, P. P.: A variational inverse method for the reconstruction of general circulation fields in the northern Bering Sea, *J. Geophys. Res.*, 96(C3), 4891, doi:10.1029/90jc02387, 1991.

914 Buga, L., Eilola, K., Wesslander, K., Fryberg, L., Gatti, J., Leroy, D., Iona, S., Tsompanou, M. and Lipizer, M.: EMODnet Thematic Lot n° 4 / SI2 . 749773 Interpolating Variational Analysis (DIVA). Release 2018, , doi:10.6092/A8CFB472-10DB-4225-9737-5A60DA9AF523, 2019.

915 Capet, A., Troupin, C., Carstensen, J., Grégoire, M. and Beckers, J. M.: Untangling spatial and temporal trends in the variability of the Black Sea Cold Intermediate Layer and mixed Layer Depth using the DIVA detrending procedure, *Ocean Dyn.*, 64(3), 315–324, doi:10.1007/s10236-013-0683-4, 2014.

916 Crispi, G., Mosetti, R., Solidoro, C. and Crise, A.: Nutrients cycling in Mediterranean basins: The role of the biological pump in the trophic regime, in *Ecological Modelling*, vol. 138, pp. 101–114., 2001.

917 Crombet, Y., Leblanc, K., Quéuiner, B., Moutin, T., Rimmelin, P., Ras, J., Claustre, H., Leblond, N., Oriol, L. and Pujo-Pay, M.: Deep silicon maxima in the stratified oligotrophic Mediterranean Sea, *Biogeosciences*, 8(2), 459–475, doi:10.5194/bg-8-459-2011, 2011.

918 de Fommervault, O. P., Migon, C., D'Ortenzio, F., Ribera d'Alcalà, M. and Coppola, L.: Temporal variability of nutrient concentrations in the northwestern Mediterranean sea (DYFAMED time-series station), *Deep. Res. Part I Oceanogr. Res. Pap.*, 100, 1–12, doi:10.1016/j.dsr.2015.02.006, 2015.

919 D'Ortenzio, F. and Ribera d'Alcalà, M.: On the trophic regimes of the Mediterranean Sea: a satellite analysis, *Biogeosciences Discuss.*, 5(4), 2959–2983, doi:10.5194/bgd-5-2959-2008, 2009.

920 D'Ortenzio, F., Taillardier, V., Claustre, H., Prieur, L. M., Leymarie, E., Mignot, A., Poteau, A.,

946 Penkerc, C. and Schmechtig, C. M.: Biogeochemical Argo : The Test Case of the NAOS Mediterranean
947 Array, , 7(March), 1–16, doi:10.3389/fmars.2020.00120, 2020.

948 DeMaster, D. J.: The accumulation and cycling of biogenic silica in the Southern Ocean: Revisiting the
949 marine silica budget, Deep. Res. Part II Top. Stud. Oceanogr., 49(16), 3155–3167, doi:10.1016/S0967-
950 0645(02)00076-0, 2002.

951 Desroziers, G., Berre, L., Chapnik, B. and Poli, P.: Diagnosis of observation, background and analysis-
952 error statistics in observation space, Q. J. R. Meteorol. Soc., 131(613), 3385–3396,
953 doi:10.1256/qj.05.108, 2005.

954 Diaz, P., Raimbault, F., Boudjellal, B., Garcia, N. and Moutin, T.: Early spring phosphorus limitation
955 of primary productivity in a NW Mediterranean coastal zone (Gulf of Lions), Mar. Ecol. Prog. Ser.,
956 211(McGill 1965), 51–62, doi:10.3354/meps211051, 2001.

957 Fichaut, M., Garcia, M. J., Giorgetti, A., Iona, A., Kuznetsov, A., Rixen, M. and Group, M.:
958 MEDAR/MEDATLAS 2002: A Mediterranean and Black Sea database for operational oceanography,
959 Elsevier Oceanogr. Ser., 69(C), 645–648, doi:10.1016/S0422-9894(03)80107-1, 2003.

960 Frings, P. J., Clymans, W., Fontorbe, G., De La Rocha, C. L. and Conley, D. J.: The continental Si cycle
961 and its impact on the ocean Si isotope budget, Chem. Geol., 425, 12–36,
962 doi:10.1016/j.chemgeo.2016.01.020, 2016.

963 García-Martínez, M. del C., Vargas-Yáñez, M., Moya, F., Santiago, R., Muñoz, M., Reul, A., Ramírez,
964 T. and Balbín, R.: Average nutrient and chlorophyll distributions in the western Mediterranean:
965 RADMED project, Oceanologia, 61(1), 143–169, doi:10.1016/j.oceano.2018.08.003, 2019.

966 Garcia, H. E., Weathers, K. W., Paver, C. R., Smolyar, I., Boyer, T. P., Locarnini, R. A., Zweng, M. M.,
967 Mishonov, A. V., Baranova, O. K., Seidov, D. and Reagan, J. R.: World Ocean Atlas 2018. Vol. 4:
968 Dissolved Inorganic Nutrients (phosphate, nitrate and nitrate+nitrite, silicate)., 2019.

969 Giorgi, F.: Climate change hot-spots, Geophys. Res. Lett., 33(8), 1–4, doi:10.1029/2006GL025734,
970 2006.

971 Hecht, A., Pinardi, N. and Robinson, A. R.: Currents, Water Masses, Eddies and Jets in the
972 Mediterranean Levantine Basin, J. Phys. Oceanogr., 18(10), 1320–1353, 1988.

973 Houpert, L., Durrieu de Madron, X., Testor, P., Bosse, A., D'Ortenzio, F., Bouin, M. N., Dausse, D., Le
974 Goff, H., Kunesch, S., Labaste, M., Coppola, L., Mortier, L. and Raimbault, P.: Observations of open-
975 ocean deep convection in the northwestern Mediterranean Sea: Seasonal and interannual variability of
976 mixing and deep water masses for the 2007–2013 Period, J. Geophys. Res. Ocean., 121(11), 8139–8171,
977 doi:10.1002/2016JC011857, 2016.

978 Key, R. M., Kozyr, A., Sabine, C. L., Lee, K., Wanninkhof, R., Bullister, J. L., Feely, R. A., Millero, F.
979 J., Mordy, C. and Peng, T. H.: A global ocean carbon climatology: Results from Global Data Analysis
980 Project (GLODAP), Global Biogeochem. Cycles, 18(4), 1–23, doi:10.1029/2004GB002247, 2004.

981 Krom, M. D., Oceanographic, I. and Shikmona, T.: Nutrient budget for the Eastern Mediterranean :
982 Implications for phosphorus limitation, , 49(5), 1582–1592, 2004.

983 Krom, M. D., Emeis, K. C. and Van Cappellen, P.: Why is the Eastern Mediterranean phosphorus
984 limited?, Prog. Oceanogr., 85(3–4), 236–244, doi:10.1016/j.pocean.2010.03.003, 2010.

985 Krom, M. D., Kress, N. and Fanning, K.: Silica cycling in the ultra-oligotrophic eastern Mediterranean
986 Sea, Biogeosciences, 11(15), 4211–4223, doi:10.5194/bg-11-4211-2014, 2014.

987 Lascaratos, A., Roether, W. and Nittis, K.: Recent changes in deep water formation and spreading in the
988 eastern Mediterranean Sea : a review, , 44, 5–36, 1999.

989 Lauvset, S. K., Key, R. M., Olsen, A., Van Heuven, S., Velo, A., Lin, X., Schirnick, C., Kozyr, A.,
990 Tanhua, T., Hoppema, M., Jutterström, S., Steinfeldt, R., Jeansson, E., Ishii, M., Perez, F. F., Suzuki, T.

991 and Watelet, S.: A new global interior ocean mapped climatology: The $1^\circ \times 1^\circ$ GLODAP version 2,
992 *Earth Syst. Sci. Data*, 8(2), 325–340, doi:10.5194/essd-8-325-2016, 2016.

993 Lauvset, S. K., Lange, N., Tanhua, T., Bittig, H. C., Olsen, A., Kozyr, A., Álvarez, M., Becker, S.,
994 Brown, P. J., Carter, B. R., Cotrim da Cunha, L., Feely, R. A., van Heuven, S., Hoppema, M., Ishii, M.,
995 Jeansson, E., Jutterström, S., Jones, S. D., Karlsen, M. K., Lo Monaco, C., Michaelis, P., Murata, A.,
996 Pérez, F. F., Pfeil, B., Schirnick, C., Steinfeldt, R., Suzuki, T., Tilbrook, B., Velo, A., Wanninkhof, R.,
997 Woosley, R. J., and Key, R. M.: An updated version of the global interior ocean biogeochemical data
998 product, GLODAPv2.2021, *Earth Syst. Sci. Data Discuss.* [preprint], <https://doi.org/10.5194/essd-2021-234>, in review, 2021.

1000 Lavigne, H.: On the vertical distribution of the chlorophyll a concentration in the Mediterranean Sea : a
1001 basin scale and seasonal approach, , (March), doi:10.5194/bgd-12-4139-2015, 2015.

1002 Lazzari, P., Solidoro, C., Ibello, V., Salon, S., Teruzzi, A., Béranger, K., Colella, S. and Crise, A.:
1003 Seasonal and inter-annual variability of plankton chlorophyll and primary production in the
1004 Mediterranean Sea: A modelling approach, *Biogeosciences*, 9(1), 217–233, doi:10.5194/bg-9-217-2012,
1005 2012.

1006 Lazzari, P., Solidoro, C., Salon, S. and Bolzon, G.: Spatial variability of phosphate and nitrate in the
1007 Mediterranean Sea: A modeling approach, *Deep. Res. Part I Oceanogr. Res. Pap.*, 108, 39–52,
1008 doi:10.1016/j.dsr.2015.12.006, 2016.

1009 Levitus, S.: Climatological Atlas of the World Ocean, *Eos, Trans. Am. Geophys. Union*, 64(49), 962–
1010 963, doi:10.1029/EO064i049p00962-02, 1982.

1011 Li, P. and Tanhua, T.: Recent Changes in Deep Ventilation of the Mediterranean Sea; Evidence From
1012 Long-Term Transient Tracer Observations, *Front. Mar. Sci.*, 7(July), 1–23,
1013 doi:10.3389/fmars.2020.00594, 2020.

1014 Lijing, C., Abraham, J., Trenberth, K. E., Fasullo, J., Boyer, T., Locarnini, R., Zhang, B., Yu, F., Wan,
1015 L., Chen, X., Song, X., Liu, Y., Mann, M.E., Reseghetti, F., Simoncelli, S., Gouretski, V., Chen, G.,
1016 Mishonov, A., Reagan, J. and Zhu, J.: Upper ocean temperatures hit record high in 2020, *Adv. Atmos.*
1017 *Sci.*, 38(4), 523–530, <https://doi.org/10.1007/s00376-021-0447-x>, 2021.

1018 Lipizer, M., Partescano, E., Rabitti, A., Giorgetti, A. and Crise, A.: Qualified temperature, salinity and
1019 dissolved oxygen climatologies in a changing Adriatic Sea, *Ocean Sci.*, 10(5), 771–797, doi:10.5194/os-
1020 10-771-2014, 2014.

1021 Lucea, A., Duarte, C. M. and Agustí, S.: Nutrient (N , P and Si) and carbon partitioning in the stratified
1022 NW Mediterranean, , 49, 157–170, doi:10.1016/S1385-1101(03)00005-4, 2003.

1023 Ludwig, W., Dumont, E., Meybeck, M. and Heussner, S.: River discharges of water and nutrients to the
1024 Mediterranean and Black Sea: Major drivers for ecosystem changes during past and future decades?,
1025 *Prog. Oceanogr.*, 80(3–4), 199–217, doi:10.1016/j.pocean.2009.02.001, 2009.

1026 Ludwig, W., Bouwman, A. F., Dumont, E. and Lespinas, F.: Water and nutrient fluxes from major
1027 Mediterranean and Black Sea rivers: Past and future trends and their implications for the basin-scale
1028 budgets, *Global Biogeochem. Cycles*, 24(4), 1–14, doi:10.1029/2009GB003594, 2010.

1029 Maillard, C., Lowry, R., Maudire, G. and Schaap, D.: SeaDataNet: Development of a Pan-European
1030 infrastructure for ocean and marine data management, in *OCEANS 2007 - Europe.*, 2007.

1031 Malanotte-Rizzoli, P., Manca, B. B., D'Alcala, M. R., Theocharis, A., Brenner, S., Budillon, G. and
1032 Ozsoy, E.: The Eastern Mediterranean in the 80s and in the 90s: The big transition in the intermediate
1033 and deep circulations, *Dyn. Atmos. Ocean.*, 29(2–4), 365–395, doi:10.1016/S0377-0265(99)00011-1,
1034 1999.

1035 Manca, B., Burca, M., Giorgetti, A., Coatanoan, C., Garcia, M. J. and Iona, A.: Physical and biochemical
1036 averaged vertical profiles in the Mediterranean regions: An important tool to trace the climatology of
1037 water masses and to validate incoming data from operational oceanography, *J. Mar. Syst.*, 48(1–4), 83–

1038 116, doi:10.1016/j.jmarsys.2003.11.025, 2004.

1039 Míguez, B. M., Novellino, A., Vinci, M., Claus, S., Calewaert, J. B., Vallius, H., Schmitt, T., Pititto, A.,
1040 Giorgetti, A., Askew, N., Iona, S., Schaap, D., Pinardi, N., Harpham, Q., Kater, B. J., Populus, J., She,
1041 J., Palazov, A. V., McMeel, O., Oset, P., Lear, D., Manzella, G. M. R., Gorringe, P., Simoncelli, S.,
1042 Larkin, K., Holdsworth, N., Arvanitidis, C. D., Jack, M. E. M., Chaves Montero, M. del M., Herman, P.
1043 M. J. and Hernandez, F.: The European Marine Observation and Data Network (EMODnet): Visions
1044 and roles of the gateway to marine data in Europe, *Front. Mar. Sci.*, 6(JUL), 1–24,
1045 doi:10.3389/fmars.2019.00313, 2019.

1046 Moon, J., Lee, K., Tanhua, T., Kress, N. and Kim, I.: Temporal nutrient dynamics in the Mediterranean
1047 Sea in response to anthropogenic inputs, , 5243–5251, doi:10.1002/2016GL068788. Received, 2016.

1048 Moore, C. M., Mills, M. M., Arrigo, K. R., Berman-Frank, I., Bopp, L., Boyd, P. W., Galbraith, E. D.,
1049 Geider, R. J., Guieu, C., Jaccard, S. L., Jickells, T. D., La Roche, J., Lenton, T. M., Mahowald, N. M.,
1050 Marañón, E., Marinov, I., Moore, J. K., Nakatsuka, T., Oschlies, A., Saito, M. A., Thingstad, T. F.,
1051 Tsuda, A. and Ulloa, O.: Processes and patterns of oceanic nutrient limitation, *Nat. Geosci.*, 6(9), 701–
1052 710, doi:10.1038/ngeo1765, 2013.

1053 Murphy, A. H.: Skill Scores Based on the Mean Square Error and Their Relationships to the Correlation
1054 Coefficient, *Mon. Weather Rev.*, 116(12), 2417–2424, doi:10.1175/1520-
1055 0493(1988)116<2417:SSBOTM>2.0.CO;2, 1988.

1056 Olsen, A., Lange, N., Key, R. M., Tanhua, T., Bittig, H. C., Kozyr, A., Álvarez, M., Azetsu-Scott, K.,
1057 Becker, S., Brown, P. J., Carter, B. R., Cotrim da Cunha, L., Feely, R. A., van Heuven, S., Hoppema,
1058 M., Ishii, M., Jeansson, E., Jutterström, S., Landa, C. S., Lauvset, S. K., Michaelis, P., Murata, A., Pérez,
1059 F. F., Pfeil, B., Schirnick, C., Steinfeldt, R., Suzuki, T., Tilbrook, B., Velo, A., Wanninkhof, R., and
1060 Woosley, R. J.: An updated version of the global interior ocean biogeochemical data product,
1061 GLODAPv2.2020, *Earth Syst. Sci. Data*, 12, 3653–3678, <https://doi.org/10.5194/essd-12-3653-2020>,
1062 2020.

1063 Ozer, T., Gertman, I., Kress, N., Silverman, J. and Herut, B.: Interannual thermohaline (1979–2014) and
1064 nutrient (2002–2014) dynamics in the Levantine surface and intermediate water masses, SE
1065 Mediterranean Sea, *Glob. Planet. Change*, doi:10.1016/j.gloplacha.2016.04.001, 2017.

1066 Piñeiro, S., González-Pola, C., Fernández-Díaz, J. M. and Balbin, R.: Thermohaline Evolution of the
1067 Western Mediterranean Deep Waters Since 2005: Diffusive Stages and Interannual Renewal Injections,
1068 *J. Geophys. Res. Ocean.*, 124(12), 8747–8766, doi:10.1029/2019JC015094, 2019.

1069 Pondaven, P., Ruiz-Pino, D., Druon, J. N., Fravalo, C. and Tréguer, P.: Factors controlling silicon and
1070 nitrogen biogeochemical cycles in high nutrient, low chlorophyll systems (the Southern Ocean and the
1071 North Pacific): Comparison with a mesotrophic system (the North Atlantic), *Deep. Res. Part I Oceanogr.*
1072 *Res. Pap.*, 46(11), 1923–1968, doi:10.1016/S0967-0637(99)00033-3, 1999.

1073 Pujo-Pay, M., Conan, P., Oriol, L., Cornet-Barthaux, V., Falco, C., Ghiglione, J. F., Goyet, C., Moutin,
1074 T. and Prieur, L.: Integrated survey of elemental stoichiometry (C, N, P) from the western to eastern
1075 Mediterranean Sea, *Biogeosciences*, 8(4), 883–899, doi:10.5194/bg-8-883-2011, 2011.

1076 Rahav, E., Herut, B., Stambler, N., Bar-Zeev, E., Mulholland, M. R. and Berman-Frank, I.: Uncoupling
1077 between dinitrogen fixation and primary productivity in the eastern Mediterranean Sea, *J. Geophys. Res.*
1078 *Biogeosciences*, 118(1), 195–202, doi:10.1002/jgrg.20023, 2013.

1079 Reale, M., Giorgi, F., Solidoro, C., Di Biagio, V., Di Sante, F., Mariotti, L., Farneti, R. and Sannino, G.:
1080 The Regional Earth System Model RegCM-ES: Evaluation of the Mediterranean climate and marine
1081 biogeochemistry., 2020.

1082 Reul, A., Rodríguez, V., Jiménez-Gómez, F., Blanco, J. M., Bautista, B., Sarhan, T., Guerrero, F., Ruíz,
1083 J. and García-Lafuente, J.: Variability in the spatio-temporal distribution and size-structure of
1084 phytoplankton across an upwelling area in the NW-Alboran Sea, (W-Mediterranean), *Cont. Shelf Res.*,
1085 25(5–6), 589–608, doi:10.1016/j.csr.2004.09.016, 2005.

1086 Ribera d'Alcalà, M.: Nutrient ratios and fluxes hint at overlooked processes in the Mediterranean Sea,
1087 *J. Geophys. Res.*, 108(C9), doi:10.1029/2002jc001650, 2003.

1088 Ribera d'Alcalà, M., Civitarese, G., Conversano, F. and Lavezza, R.: Nutrient ratios and fluxes hint at
1089 overlooked processes in the Mediterranean Sea, *J. Geophys. Res. Ocean.*, 108(9),
1090 doi:10.1029/2002jc001650, 2003.

1091 Rixen, M., Beckers, J. M., Brankart, J. M. and Brasseur, P.: A numerically efficient data analysis method
1092 with error map generation, *Ocean Model.*, 2(1–2), 45–60, doi:10.1016/s1463-5003(00)00009-3, 2000.

1093 Roether, W. and Schlitzer, R.: Eastern Mediterranean deep water renewal on the basis of
1094 chlorofluoromethane and tritium data, *Dyn. Atmos. Ocean.*, 15(3–5), 333–354, doi:10.1016/0377-
1095 0265(91)90025-B, 1991.

1096 Roether, W., Manca, Beniamino B. Klein, B., Bregant, D., Georgopoulos, D., Beitzel, V. and
1097 KovaEevic, Vedrana Luchetta, A.: Recent Changes in Eastern Mediterranean Deep Waters., 1996.

1098 Roether, W., Klein, B., Bruno, B., Theocharis, A. and Kioroglou, S.: Progress in Oceanography
1099 Transient Eastern Mediterranean deep waters in response to the massive dense-water output of the
1100 Aegean Sea in the 1990s, , 74, 540–571, doi:10.1016/j.pocean.2007.03.001, 2007.

1101 Roether, W., Klein, B. and Hainbucher, D.: The Eastern Mediterranean Transient: Evidence for Similar
1102 Events Previously?, *Mediterr. Sea Temporal Var. Spat. Patterns*, 9781118847(January), 75–83,
1103 doi:10.1002/9781118847572.ch6, 2014.

1104 Salgado-Hernanz, P. M., Racault, M. F., Font-Muñoz, J. S. and Basterretxea, G.: Trends in
1105 phytoplankton phenology in the Mediterranean Sea based on ocean-colour remote sensing, *Remote
1106 Sens. Environ.*, 221(October 2018), 50–64, doi:10.1016/j.rse.2018.10.036, 2019.

1107 Sarmiento, J. L. and Toggweiler, J. R.: A new model for the role of the oceans in determining
1108 atmospheric PCO₂, *Nature*, 308(5960), 621–624, doi:10.1038/308621a0, 1984.

1109 Schröder, K., Gasparini, G. P., Tangherlini, M. and Astraldi, M.: Deep and intermediate water in the
1110 western Mediterranean under the influence of the Eastern Mediterranean Transient, *Geophys. Res. Lett.*,
1111 33(21), 2–7, doi:10.1029/2006GL027121, 2006.

1112 Schroeder, K., Gasparini, G. P., Borghini, M., Cerrati, G. and Delfanti, R.: Biogeochemical tracers and
1113 fluxes in the Western Mediterranean Sea , spring 2005, *J. Mar. Syst.*, 80(1–2), 8–24,
1114 doi:10.1016/j.jmarsys.2009.08.002, 2010.

1115 Schroeder, K., Tanhua, T., Bryden, H., Alvarez, M., Chiggiato, J. and Aracri, S.: Mediterranean Sea
1116 Ship-based Hydrographic Investigations Program (Med-SHIP), *Oceanography*, 28(3), 12–15,
1117 doi:10.5670/oceanog.2015.71, 2015.

1118 Schroeder, K., Chiggiato, J., Bryden, H. L., Borghini, M. and Ismail, S. Ben: Abrupt climate shift in the
1119 Western Mediterranean Sea, *Nat. Publ. Gr.*, 1–7, doi:10.1038/srep23009, 2016.

1120 Schroeder, K., Chiggiato, J., Josey, S. A., Borghini, M., Aracri, S. and Sparnocchia, S.: Rapid response
1121 to climate change in a marginal sea, , (May), 1–7, doi:10.1038/s41598-017-04455-5, 2017.

1122 Schroeder, K., Cozzi, S., Belgacem, M., Borghini, M., Cantoni, C., Durante, S., Petrizzo, A., Poiana, A.
1123 and Chiggiato, J.: Along-Path Evolution of Biogeochemical and Carbonate System Properties in the
1124 Intermediate Water of the Western Mediterranean, *Front. Mar. Sci.*, 7(May), 1–19,
1125 doi:10.3389/fmars.2020.00375, 2020.

1126 Shepherd, J. G., Brewer, P. G., Oschlies, A. and Watson, A. J.: Ocean ventilation and deoxygenation in
1127 a warming world: posters, *Philos. Trans. R. Soc. A Math. Phys. Eng. Sci.*, 375(2102), 20170241,
1128 doi:10.1098/rsta.2017.0241, 2017.

1129 Sospedra, J., Niencheski, L. F. H., Falco, S., Andrade, C. F. F., Attisano, K. K. and Rodilla, M.:
1130 ScienceDirect Identifying the main sources of silicate in coastal waters of the Southern Gulf of Valencia

1131 (Western Mediterranean Sea), *Oceanologia*, 60(1), 52–64, doi:10.1016/j.oceano.2017.07.004, 2018.

1132 Stöven, T. and Tanhua, T.: Ventilation of the mediterranean sea constrained by multiple transient tracer
1133 measurements, *Ocean Sci.*, 10(3), 439–457, doi:10.5194/os-10-439-2014, 2014.

1134 Tanhua, T., Hainbucher, D., Schroeder, K., Cardin, V., Álvarez, M. and Civitarese, G.: The
1135 Mediterranean Sea system: A review and an introduction to the special issue, *Ocean Sci.*, 9(5), 789–
1136 803, doi:10.5194/os-9-789-2013, 2013.

1137 Testor, P., Bosse, A., Houpert, L., Margirier, F., Mortier, L., Legoff, H., Dausse, D., Labaste, M.,
1138 Karstensen, J., Hayes, D., Olita, A., Ribotti, A., Schroeder, K., Chiggiato, J., Onken, R., Heslop, E.,
1139 Mourre, B., D'ortenzio, F., Mayot, N., Lavigne, H., de Fommervault, O., Coppola, L., Prieur, L.,
1140 Taillandier, V., Durrieu de Madron, X., Bourrin, F., Many, G., Damien, P., Estournel, C., Marsaleix, P.,
1141 Taupier-Letage, I., Raimbault, P., Waldman, R., Bouin, M. N., Giordani, H., Caniaux, G., Somot, S.,
1142 Ducrocq, V. and Conan, P.: Multiscale Observations of Deep Convection in the Northwestern
1143 Mediterranean Sea During Winter 2012–2013 Using Multiple Platforms, *J. Geophys. Res. Ocean.*,
1144 123(3), 1745–1776, doi:10.1002/2016JC012671, 2018.

1145 Theocharis, A., Lascaratos, A. and Sofianos, S.: Variability of sea water properties in the Ionian , Cretan
1146 and Levantine seas during the last century, , (April), 22–24, 2002.

1147 Troupin, C., MacHín, F., Ouberrous, M., Sirjacobs, D., Barth, A. and Beckers, J. M.: High-resolution
1148 climatology of the northeast Atlantic using Data-Interpolating Variational Analysis (Diva), *J. Geophys.*
1149 *Res. Ocean.*, 115(8), 1–20, doi:10.1029/2009JC005512, 2010.

1150 Troupin, C., Barth, A., Sirjacobs, D., Ouberrous, M., Brankart, J. M., Brasseur, P., Rixen, M., Alvera-
1151 Azcárate, A., Belounis, M., Capet, A., Lenartz, F., Toussaint, M. E. and Beckers, J. M.: Generation of
1152 analysis and consistent error fields using the Data Interpolating Variational Analysis (DIVA), *Ocean*
1153 *Model.*, 52–53, 90–101, doi:10.1016/j.ocemod.2012.05.002, 2012.

1154 Troupin, C., Watelet, S., Ouberrous, M., Sirjacobs, D., Barth, A., Toussaint, M. and Beckers, J.: Data
1155 Interpolating Variational Analysis User Guide, , 836723, doi:10.5281/zenodo.836723, 2018.

1156 Van Cappellen, P., Powley, H. R., Emeis, K. C. and Krom, M. D.: A biogeochemical model for
1157 phosphorus and nitrogen cycling in the Eastern Mediterranean Sea: Part 1: Model development,
1158 initialization and sensitivity, *J. Mar. Syst.*, 139, 460–471, doi:10.1016/j.jmarsys.2014.08.016, 2014.

1159 Vargas-yáñez, M.: Updating temperature and salinity mean values and trends in the Western
1160 Mediterranean : The RADMED project Progress in Oceanography Updating temperature and salinity
1161 mean values and trends in the Western Mediterranean : The RADMED project, *Prog. Oceanogr.*,
1162 157(September), 27–46, doi:10.1016/j.pocean.2017.09.004, 2017.

1163 Weatherall, P., Marks, K. M., Jakobsson, M., Schmitt, T., Tani, S., Arndt, J. E., Rovere, M., Chayes, D.,
1164 Ferrini, V. and Wigley, R.: A new digital bathymetric model of the world's oceans, *Earth Sp. Sci.*, 2,
1165 331–345, doi:doi: 10.1002/ 2015EA000107, 2015.

1166 Williams, R. G. and Follows, M. J.: Physical Transport of Nutrients and the Maintenance of Biological
1167 Production, in *Ocean Biogeochemistry*, pp. 19–51., 2003.

1168